



HAL
open science

Estimating agricultural ammonia volatilization over Europe using satellite observations and simulation data

Rimal Abeed, Camille Viatte, William C. Porter, Nikolaos Evangeliou, Cathy Clerbaux, Lieven Clarisse, Martin van Damme, Pierre-François Coheur, Sarah Safieddine

► To cite this version:

Rimal Abeed, Camille Viatte, William C. Porter, Nikolaos Evangeliou, Cathy Clerbaux, et al.. Estimating agricultural ammonia volatilization over Europe using satellite observations and simulation data. Atmospheric Chemistry and Physics Discussions, In press, 10.5194/egusphere-2022-1046 . hal-03838661v1

HAL Id: hal-03838661

<https://hal.science/hal-03838661v1>

Submitted on 3 Nov 2022 (v1), last revised 9 Oct 2023 (v2)

HAL is a multi-disciplinary open access archive for the deposit and dissemination of scientific research documents, whether they are published or not. The documents may come from teaching and research institutions in France or abroad, or from public or private research centers.

L'archive ouverte pluridisciplinaire **HAL**, est destinée au dépôt et à la diffusion de documents scientifiques de niveau recherche, publiés ou non, émanant des établissements d'enseignement et de recherche français ou étrangers, des laboratoires publics ou privés.



Distributed under a Creative Commons Attribution 4.0 International License



1 Estimating agricultural ammonia volatilization over Europe 2 using satellite observations and simulation data

3 Rimal Abeed¹, Camille Viatte¹, William C. Porter², Nikolaos Evangeliou³, Cathy Clerbaux^{1,4},
4 Lieven Clarisse⁴, Martin Van Damme^{4,5}, Pierre-François Coheur⁴, and Sarah Safieddine¹

6 ¹LATMOS/IPSL, Sorbonne Université, UVSQ, CNRS, Paris, France

7 ²Department of Environmental Sciences, University of California, Riverside, CA 92521, USA

8 ³Norwegian Institute for Air Research (NILU), Department of Atmospheric and Climate Research (ATMOS),
9 Kjeller, Norway

10 ⁴Université libre de Bruxelles (ULB), Spectroscopy, Quantum Chemistry and Atmospheric Remote Sensing
11 (SQUARES), Brussels, Belgium

12 ⁵Belgian Institute for Space Aeronomy (BIRA-IASB), Brussels 1180, Belgium

13

14 *Correspondence to:* Rimal Abeed rimal.abeed@latmos.ipsl.fr

15

16 Abstract

17 Ammonia (NH₃) is one of the most important gases emitted from agricultural practices. It affects air
18 quality and the overall climate, and in turn influenced by long term climate trends as well as by short term
19 fluctuations in local and regional meteorology. Previous studies have established the capability of the Infrared
20 Atmospheric Sounding Interferometer (IASI) series of instruments aboard the Metop satellites to measure
21 ammonia from space since 2007. In this study, we explore the interactions between atmospheric ammonia, land
22 and meteorological variability, and long-term climate trends in Europe. We investigate the emission potential
23 (Γ_{soil}) of ammonia from the soil, which describes the soil – atmosphere ammonia exchange. Γ_{soil} is generally
24 calculated in-field or in laboratory experiments; here, and for the first time, we investigate a method which assesses
25 it remotely using satellite data, reanalysis data products, and model simulations.

26 We focus on ammonia emission potential during March 2011, which marks the start of growing season
27 in Europe. Our results show that Γ_{soil} ranges from 2×10^3 to 9.5×10^4 (dimensionless) in a fertilized cropland,
28 such as in the North European Plain, and is of the order of $10 - 10^2$ in a non-fertilized soil (e.g. forest and grassland).
29 These results agree with in-field measurements from the literature, suggesting that our method can be used in other
30 seasons and regions in the world. However, some improvements are needed in the determination of mass transfer
31 coefficient k (m s⁻¹), which is a crucial parameter to derive Γ_{soil} .

32 Using a climate model, we estimate the expected increase in ammonia columns by the end of the century
33 based on the increase in skin temperature (T_{skin}), under two different climate scenarios. Ammonia columns are
34 projected to increase by up to 50 %, particularly in Eastern Europe, under the SSP2-4.5 scenario, and might even
35 double (increase of 100 %) under the SSP5-8.5 scenario. The increase in skin temperature is responsible for a
36 formation of new hotspots of ammonia in Belarus, Ukraine, Hungary, Moldova, parts of Romania, and
37 Switzerland.

38



39 1. Introduction

40 Ammonia (NH_3) emissions have been increasing in a continuous manner from 1970 to 2017 (McDuffie et al.,
41 2020). During the period 2008 – 2018 alone, the increase in ammonia columns in Western and Southern Europe
42 accounted to $20.8 \text{ \% yr}^{-1} (\pm 4.3 \text{ \%})$, and to $12.8 (\pm 1.3 \text{ \%})$ globally (Van Damme et al., 2021). Although ammonia
43 alone is stable against heat and light, it is considered a very reactive base, whereas it constitutes the largest portion
44 of the reactive nitrogen (N_r) on Earth. The vast majority of atmospheric ammonia not deposited is transformed into
45 fine particulate matter ($\text{PM}_{2.5}$) composed of ammonium (NH_4^+), through acid – base chemical reactions with
46 available acids in the environment, namely sulfuric acid (H_2SO_4), hydrochloric acid (HCl), and nitric acid (HNO_3)
47 (Yu et al., 2018), while only 10 % of the total ammonia gas are believed to be oxidized by hydroxyl radicals (OH^\cdot)
48 (Roelle and Aneja, 2005). $\text{PM}_{2.5}$ has degrading effects on human health, especially respiratory diseases (Bauer et
49 al., 2016). In addition to agriculture, ammonia can be emitted from industrial processes, biomass burning (Van
50 Damme et al., 2018), and natural activities such as from seal colonies (Theobald et al., 2006).

51
52 Soils are known to be a source of atmospheric ammonia, especially in areas of intensive agricultural practices
53 (Schlesinger and Hartley, 1992), and this is due to enriching the soil with the reactive nitrogen present in fertilizers.
54 The increase in the application of synthetic fertilizers, and intensification of agricultural practices is believed to be
55 the dominant factor of the global increase in ammonia emissions over the past century (Behera et al., 2013;
56 McDuffie et al., 2020).

57
58 Following the application of fertilizers, ammonium and ammonia are released in the soil. Prior to its volatilization,
59 ammonia in the soil exists either in the gas phase ($\text{NH}_{3(g)}$) or in the aqueous/liquid phase ($\text{NH}_{3(aq)}$), the equilibrium
60 between both states of ammonia is governed by Henry's law (Wentworth et al., 2014), as shown in A. The
61 dissociation of ammonia in soil water is affected by soil acidity (pH) and temperature (Roelle and Aneja, 2005)
62 (Eq. (A-1) and (A-2) in Appendix A); it is explained by the dissociation constant $K_{\text{NH}_4^+}$. Once released to the
63 atmosphere, ammonia near the surface exists in the gas phase, hence Henry's law describes the equilibrium
64 between ammonia in the soil (liquid phase), and near the surface (gas phase). This bi-directional exchange between
65 the soil and the atmosphere will continue until the equilibrium is reached, and this occurs when ammonia
66 concentration is equal to the compensation point χ_{NH_3} (the concentration of ammonia at equilibrium). The flux of
67 ammonia from the soil to the atmosphere (emission) occurs when the concentration of atmospheric ammonia is
68 less than the compensation point χ_{NH_3} , while ammonia deposition occurs when the concentration of ammonia is
69 equal to or greater than χ_{NH_3} (Flechard et al., 2011; Wichink Kruit, 2010). It is then crucial to quantify the
70 compensation point in order to understand this bi-directional exchange. The main variables needed to calculate
71 χ_{NH_3} are soil temperature (T_{skin}) and Γ_{soil} , which is a dimensionless ratio between ammonium and pH ($\text{NH}_4^+_{(aq)}$
72 and $\text{H}^+_{(aq)}$ concentrations, respectively, in the soil). All the equations are described in Appendix A (Eq. (A-1) to
73 (A-15)).

74
75 The soil emission potential (Γ_{soil}) has been thoroughly investigated in field and controlled laboratory environments
76 (e.g. David et al., 2009; Flechard et al., 2013; Massad et al., 2010; Mattsson et al., 2008; Nemitz et al., 2000;
77 Wentworth et al., 2014, among others). Γ_{soil} is dimensionless and it can range from 20 (non-fertilized soil in a
78 forest) to the order of 10^6 (mixture of slurry in a cropland). It is found to peak right after fertilizers application,
79 due to the increase in ammonium content in the soil (a product of urea hydrolysis), reaching pre-fertilization levels
80 10 days following the application (Flechard et al., 2010; Massad et al., 2010). Little information exists on regional
81 or global scales to assess the large-scale spatial variability of ammonia emission potentials.

82
83 In order to meet the needs for a growing population, agricultural practices have intensified during the period 2003
84 – 2019 (more fertilizer use per surface area), resulting in an increase in the net primary production (NPP) per capita



85 (Potapov et al., 2022), subsequently increasing volatilized ammonia (increase in nitrogen soil content, and
86 cultivated lands). In Europe alone, the area of croplands increased by 9 % from 2003 to 2019, and most of the
87 expansion took place on lands that were abandoned for more than 4 years (Potapov et al., 2022). Between the year
88 2008 and 2018, the increase in atmospheric ammonia columns accounted to 20.8 % (± 4.3 %) in Western and
89 Southern Europe (Van Damme et al., 2021). With the increase in croplands area and agricultural activities, climate
90 change will have a significant effect on agricultural practices, with warmer climates enhancing the volatilization
91 of ammonia from soils, especially in intensely fertilized lands (Shen et al., 2020).

92
93 This study aims at exploring ammonia emission potential/volatilization in Europe, using infrared satellite data of
94 ammonia columns, reanalysis temperature data, and chemical transport model simulations to provide information
95 on chemical sources and sinks. We specifically study the relationship between satellite-derived ammonia
96 concentration at the start of the growing season, soil emission potentials and their spatial variability over Europe
97 during March of 2011. Section 2 provides the methods/datasets used. Simulation results are described in Sect. 3,
98 and regional emission potentials are shown and discussed in Sect. 4. Using a climate model, future projections of
99 ammonia columns are investigated under different climate scenarios in Sect. 5. Discussion and conclusions are
100 listed in Sect. 6.

101 2. Methodology

102 2.1. Calculation of the emission potential

103
104 In this study, we use IASI satellite data to calculate the ammonia emission potential Γ_{soil} instead of field soil
105 measurements. In field studies, Γ_{soil} is calculated by measuring the concentration of ammonium (NH_4^+) and H^+
106 ($10^{-\text{pH}}$) in the soil; the ratio between both of these concentrations is Γ_{soil} . In this study, we use infrared satellite
107 ammonia to have a regional coverage over Europe. With these, we cannot monitor soil content of ammonium nor
108 its pH. This renders the remote Γ_{soil} calculation challenging, and less straight forward. The full derivation of the
109 equation used to calculate the emission potential is explained in Appendix A, and was briefly described in the
110 introduction. In short, upon its dissolution in the soil water, ammonia follows Henry's law. In steady state
111 conditions between the soil and the near surface, the amount of the ammonia emitted and lost is considered equal.
112 Based on this assumption, the soil emission potential (dimensionless) is calculated as follows Eq. (2-1) or Eq. (A-
113 15) in Appendix A:

$$114 \Gamma_{soil} = \frac{[\text{NH}_3]^{col} \cdot T_{soil}}{\exp\left(\frac{-b}{T_{soil}}\right)} \frac{M_{\text{NH}_3}}{a \cdot N_a \cdot c'} \cdot \frac{1}{k\tau} \quad (2-1)$$

115
116 Where $[\text{NH}_3]^{col}$ is the total column concentration of ammonia (molecules cm^{-2}), measured by satellite remote
117 sensors, T_{soil} is the soil temperature at the surface, which can be expressed as the skin temperature, T_{skin} (Kelvin),
118 a and b are constants ($a = 2.75 \times 10^3 \text{ g K cm}^{-3}$, $b = 1.04 \times 10^4 \text{ K}$), M_{NH_3} is the molar mass of ammonia gas
119 ($M = 17.031 \text{ g mol}^{-1}$), and N_a is Avogadro's number ($N_a = 6.0221409 \times 10^{23} \text{ molecules mol}^{-1}$), c' is
120 equals to 100 and is added to convert k from m s^{-1} to cm s^{-1} (since $[\text{NH}_3]^{col}$ is in molecules cm^{-1}), and τ the lifetime
121 of ammonia (seconds).

122 k is the soil – atmosphere exchange coefficient or deposition velocity (cm s^{-1}), also known as the mass transfer
123 coefficient (this nomenclature will be used in this study). It is found to be affected by the roughness length of the
124 surface, wind speed, the boundary layer height (Olesen and Sommer, 1993; Van Der Molen et al., 1990), and pH



125 (Lee et al., 2020). It can be explained by a resistance model often used to explain the exchange between the surface
126 and the atmosphere (Wentworth et al., 2014). Different studies provide look up tables values of k for different land
127 cover types and different seasons based on this resistance model (Aneja et al., 1986; Erisman et al., 1994; Phillips
128 et al., 2004; Roelle and Aneja, 2005; Svensson and Ferm, 1993; Wesely, 1989).
129 In general, the mass transfer coefficient k is in the order of 10^{-3} to 10^{-2} m s^{-1} in a mixture of soil and manure, and
130 10^{-6} to 10^{-5} m s^{-1} in a mixture of manure alone (Roelle and Aneja, 2005). We discuss and provide more information
131 on k in Sect. 4, and additional details on this calculation in general are provided in Appendix A.
132

133 2.2. IASI ammonia, ERA5 T skin, and MODIS Land cover

134
135 The Infrared Atmospheric Sounding Interferometer (IASI) is considered advanced the most innovative
136 instrument onboard the polar-orbiting Metop satellites (Klaes, 2018). Three IASI instruments are onboard Metop-
137 A, B and C, the series of satellites launched by the EUMETSAT (European Organization for the Exploitation of
138 Meteorological Satellites) in 2006, 2012, and 2018, respectively. The Metop-A satellite was de-orbited in October
139 2021 (Lentze, 2021), and as a result only two instruments (IASI-B and C onboard Metop-B and C) are operating
140 today. The observations from IASI cover any location on Earth at 9:30 in the morning (AM) and in the evening
141 (PM), local solar time. It can detect a variety of atmospheric species including trace gases (Clerbaux et al., 2009).
142 The IASI Fourier-transform spectrometer monitors the atmosphere in the spectral range between 645 and 2760
143 cm^{-1} (thermal infrared), and is nadir-looking. IASI has a swath width that measures 2200 km, with a pixel size of
144 ~ 12 km.
145

146 Ammonia was first detected with IASI using the ν_2 vibrational band of ammonia (~ 950 cm^{-1}) (Clerbaux et al.,
147 2009; Coheur et al., 2009). The ammonia total columns used in this study are the product of an Artificial Neural
148 Network and re-analyzed temperature data from the European Centre for Medium-Range Weather Forecasts
149 (ECMWF) product ERA5 ANNI-NH₃-v3R-ERA5 (Van Damme et al., 2021). Several studies used ammonia data
150 from IASI to study hotspots of ammonia of different source types including both natural and anthropogenic sources
151 (Clarisse, Van Damme, Clerbaux, et al., 2019; Clarisse, Van Damme, Gardner, et al., 2019; Dammers et al., 2019;
152 Van Damme et al., 2018, 2021; Viatte et al., 2021). Recently, IASI observations were used to study the effect of
153 war and conflict on agricultural practices in Syria (Abeed et al., 2021).
154

155 Fewer errors on the retrieval were observed during the day and over land (Van Damme et al., 2017), hence, we
156 use only daytime ammonia measurements from IASI. Comparisons with ammonia measured using a ground-based
157 instrument showed a good correlation of $R=0.75$ (Viatte et al., 2021). Satellite ammonia data from CrIS (Crosstrack
158 Infrared Sounder) (Shephard and Cady-Pereira, 2015) were compared with those from IASI, and were equally
159 found to give similar results when looking at concentrations from a wildfire (Adams et al., 2019), showing
160 consistency when studying seasonal and inter-annual variability (Viatte et al., 2020).
161

162 In addition to ammonia, we look at skin temperature (T_{skin} or land surface temperature LST) data from the
163 ECMWF reanalysis (ERA5) at a grid resolution of $0.25 \times 0.25^\circ$ (Hersbach et al., 2020). ERA5 Temperatures are
164 interpolated temporally and spatially to the IASI morning overpass ($\sim 9:30$ A.M. local time), since we only consider
165 daytime ammonia. ERA5 temperature data are also used in the retrieval process of the ammonia data we used in
166 this study NH₃-v3R-ERA5 (Van Damme et al., 2021). T_{skin} is defined as the temperature of the uppermost surface
167 layer when radiative equilibrium is reached. It also represents the theoretical temperature required in order to reach
168 the surface energy balance (ECMWF, 2016).
169



170 In order to assign a mass transfer coefficient k to each land type, the moderate resolution imaging
171 spectroradiometer (MODIS), a series of instruments orbiting the Earth aboard the Aqua and Terra satellites, is
172 used. The data product MCD12Q1 (version 6) is a combined Aqua/Terra Land cover type product, with a spatial
173 resolution of 500 m. This product provides maps of land cover type from 2001 through 2019 (Sulla-Menashe and
174 Friedl, 2018). From the land use categories included in the MOD12Q1 product (Belward et al., 1999) we focus on
175 croplands, forests, shrublands, and grasslands. We do not include barelands, snow cover, and urban areas in our
176 analysis; we are not interested in studying these surfaces, since we focus on ammonia volatilization from the soil
177 in areas amended with fertilizers. We show the emission potential in Forests and grasslands/shrublands for
178 comparison with values in the literature. In an attempt to calculate an emission potential (Eq. (2-1)) that is relevant
179 to the land cover/use, we therefore assign a mass transfer coefficient k to each land type based on literature values
180 (Aneja et al., 1986; Erisman et al., 1994; Roelle and Aneja, 2005; Svensson and Ferm, 1993; Wesely, 1989) and
181 we discuss it in Sect. 4.
182

183 **2.3. Model simulations**

184 **2.3.1. GEOS-Chem Chemistry Transport Model**

185
186 In this study we use version 12.7.2 of the GEOS-Chem chemical transport model (Bey et al., 2001). The model is
187 driven by the Modern-Era Retrospective Analysis for Research and Applications version 2 (MERRA-2) reanalysis
188 product, including nested domains over Europe at a $0.5^\circ \times 0.625^\circ$ horizontal resolution. MERRA-2 is the second
189 version of the MERRA atmospheric reanalysis product by NASA Global Modulation Assimilation Office
190 (NASA/GMAO) (Gelaro et al., 2017). Boundary conditions for the nested domains are created using a global
191 simulation for the same months at $2^\circ \times 2.5^\circ$ resolution. We generate model output for March of 2011, preceded by
192 a one month of discarded model spin-up time for the nested run, and two months for the global simulation. March
193 corresponds well to the month of fertilizer application in Europe, and as such to the beginning of the growing
194 season (FAO, 2022; USDA, 2022).
195

196 Output includes the monthly mean for selected diagnostics. Anthropogenic emissions are taken primarily from the
197 global Community Emissions Data System (CEDS) inventory (Hoesly et al., 2018). Biogenic non-agricultural
198 ammonia, as well as ocean ammonia sources, are taken from the Global Emission Inventories Activities database
199 (GEIA, (Bouwman et al., 1997)). Open fire emissions are generated using the GFED 4.1s inventory (Randerson et
200 al., 2015). We used the Harmonized Emissions Component module (HEMCO) to obtain the ammonia emissions
201 over Europe (Keller et al., 2014).
202

203 **2.3.2. EC-Earth Climate model**

204 To analyze how future climate will affect ammonia concentration and emission potential, we use the ECMWF
205 climate model the European Earth Consortium climate model (EC-Earth, <http://www.ec-earth.org/>). While other
206 climate models exist, we choose this one because the ammonia product from IASI uses ERA5 for the retrievals
207 and we calculate the emission potential from the T skin product of ERA5. The reanalysis uses the ECMWF
208 Integrated Forecasting System for the atmosphere–land component (IFS). IFS is also used in EC-Earth and is
209 complemented with other model components to simulate the full range of Earth system interactions that are
210 relevant to climate (Döscher et al., 2021). We note that the versions of the IFS models used in ERA5 and in EC-
211 Earth are not identical as the climate model product is not assimilated and is not initialized with observations



212 several times a day like ERA5. The EC-Earth simulations are included in the Climate model intercomparison
213 project, phase 6 (Eyring et al., 2016), part of the Intergovernmental Panel on Climate Change (IPCC) report of
214 2021 (Masson-Delmotte, et al., 2021). We use the so-called Scenario Model Intercomparison Project
215 (ScenarioMIP), covering the period [2015 – 2100] for future projections under different shared socio-economic
216 pathways (SSP) (Riahi et al., 2017). We analyze two scenarios, the SSP2-4.5 corresponding to “middle of the
217 road” socio-economic family with a nominal 4.5W/m^2 radiative forcing level by 2100 - approximately
218 corresponding to the RCP-4.5 scenario, and the SSP5-8.5 marks the upper edge of the SSP scenario spectrum with
219 a high reference scenario in a high fossil-fuel development world throughout the 21st century.

220 3. GEOS-Chem model simulation: validation and analysis

221 3.1. GEOS-Chem validation with IASI

222
223 In order to analyse how well the model simulates atmospheric ammonia, we use the simulated GEOS-Chem
224 monthly averaged (March 2011) ammonia total columns output (Sect. 2.3.1). We compare those to the IASI total
225 columns of ammonia gridded on the same horizontal resolution ($0.5^\circ \times 0.625^\circ$) and over the same month.

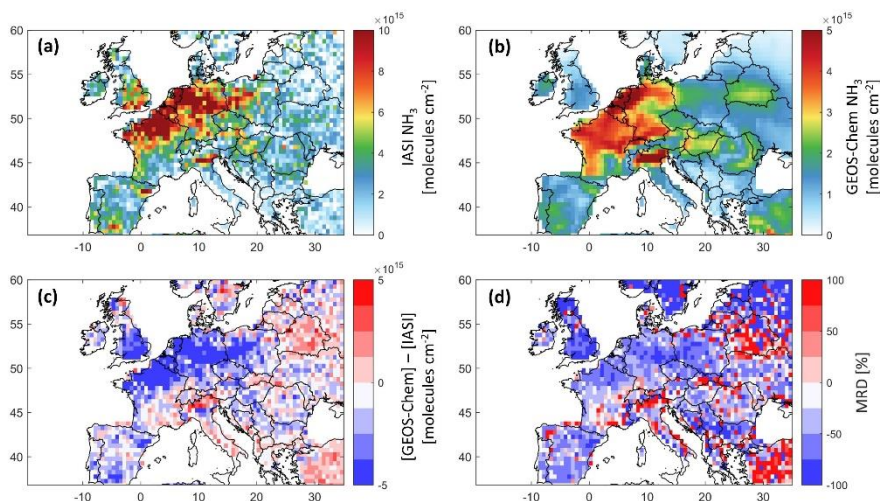


Figure 1. Ammonia total column concentrations from IASI (panel a), and GEOS-Chem (panel b), the difference between both datasets (panel c) in molecules cm^{-2} , and the Mean Relative Difference (MRD) in % (panel d); all data are a monthly average of March 2011, and over Europe at a $0.5^\circ \times 0.625^\circ$ grid resolution. Note that the colour bar limits are different between panels (a) and (b).

226
227 Figure 1 shows the IASI NH_3 distribution (Figure 1a), and that from GEOS-Chem (Figure 1b), the bias between
228 the two (Figure 1c), and the mean relative difference MRD (Figure 1d), all during March 2011. MRD is calculated
229 as the mean of the ratio $\frac{(\text{GeosChem } \text{NH}_3 - \text{IASI } \text{NH}_3) \times 100}{\text{IASI } \text{NH}_3}$ at each grid point.

230



231 Generally, both GEOS-Chem and IASI show coincident sources of ammonia, reflecting the good ability of the
232 model to reproduce ammonia columns over major agricultural source regions in Europe. The bias between IASI
233 and GEOS-Chem and the MRD are shown in Figure 1c and d. Ammonia columns from GEOS-Chem are
234 underestimated by up to 2×10^{16} molecules/cm² in some source regions/over hotspots, especially in England, North
235 Eastern France, the North European Plain (Netherlands, Belgium), and Spain (around Barcelona). Similar results
236 were found in the study of Whitburn et al. (2016), in which they show that GEOS-Chem underestimates ammonia
237 columns by up to 1×10^{16} molecules/cm² in Europe on a yearly average in 2009, notably in the North European
238 Plain. It is important to note that, in our study, we compare only one month of data (March, 2011) that marks the
239 start of the growing season in the majority of the countries of interest (FAO, 2022; USDA, 2022). The differences
240 are mainly because of the time coincidence, and the fact that only cloud-free data are used to retrieve ammonia;
241 IASI observes ammonia during the satellite overpass (~9:30 AM local time), whereas the GEOS-Chem simulation
242 is averaged over the whole month including all hours of the day. In Western and Northern Europe, the MRD is
243 mostly less than -50% , for instance, in the North European Plain (-49%). If we look at the average MRD in
244 regions of focus, we see that the Po Valley in Italy has the highest MRD value ($+110\%$), whereas the best
245 represented region is New Aquitaine in the southwest of France (-20%). The rest of the regions have mean MRDs
246 that fluctuate between -64% and -42% . A summary of the results of this study, including the MRD over some
247 source regions is listed in Table 1. Although the bias and MRD can be considered high, the spatial distribution is
248 consistent between IASI and GEOS-Chem. Therefore, according to the steady state approximation, the
249 meteorological and soil parameters affecting one dataset (e.g. IASI NH₃) are applicable to the other (e.g. model
250 simulation). It is worth noting that although we do not use the latest version of GEOS-Chem, the results we obtain
251 reflects our current understanding of the regional chemistry at this horizontal and temporal resolution.

252 **3.2. Ammonia emissions, losses and lifetime in Europe**

253 In order to understand the NH₃ spatial variability in Europe during the application of fertilizers, a detailed analysis
254 of the output of the GEOS-Chem simulation for the month of March 2011 is shown in Figure 2.

255 The anthropogenic sources (i.e. mainly agriculture) contribute 83 % of the total ammonia emissions during March
256 2011 in Europe. The ammonia emissions from natural sources (i.e. soil of natural vegetation, oceans, and wild
257 animals) follow representing 16 % of the total emissions, whereas the remaining 1 % correspond to the ammonia
258 emissions from biomass burning and ships (not shown here).

259 Figure 2a shows ammonia monthly emissions. Most of them are due to agricultural activities (not shown here); we
260 identify 8 source regions which we investigate thoroughly in this study shown as rectangles A to H. The highest
261 agricultural sources over Europe include the North European Plain, Brittany, and the Po Valley (regions C, D, and
262 F).

263 In the calculation of the total loss of ammonia (Figure 2b), we considered dry deposition, chemistry, transport, and
264 wet deposition (in which we included ammonia loss to convection) from the GEOS-Chem model simulation, which
265 are all possible loss processes for ammonia (David et al., 2009). Figure 2b shows that the largest losses occur
266 logically where we have the highest sources detected (see Figure 2a).

267
268

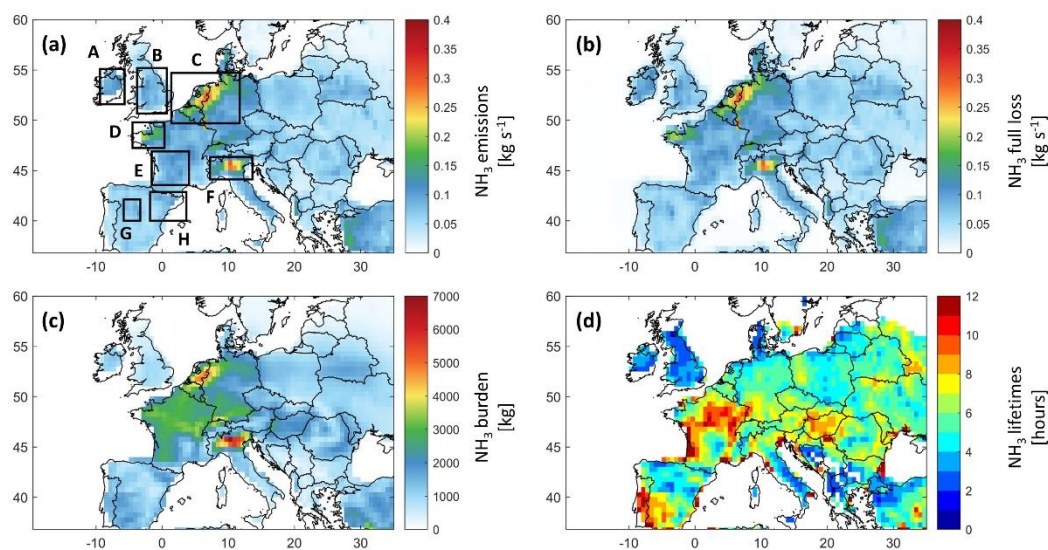


Figure 2. Ammonia budget in Europe from GEOS-Chem: (a) Ammonia emissions from the Harmonized Emissions Component module (HEMCO) in kg s^{-1} with our regions of interest shown in rectangles, (b) ammonia full loss in kg s^{-1} , (c) ammonia total burden in kg, and (d) ammonia lifetime in hours. All plots refer to March 2011 and are presented at a $0.5^\circ \times 0.625^\circ$ grid resolution.

269 The total ammonia burden (Figure 2c) is calculated as the integrated sum of all ammonia columns in the model
270 grid box. We can clearly detect ammonia hotspots over Europe, in particular the North European Plain, Brittany
271 and the Po Valley, all regions characterized by intense agricultural activities, as the total emissions and deposition
272 show (Figure 1 and Figure 2). We also see that the burden is generally the highest over France, Belgium, The
273 Netherlands, and parts of Germany and Italy.

274
275 We finally get the lifetime τ_{ss} of ammonia (Figure 2d). In the case of a gas with a short lifetime, such as ammonia,
276 the emissions are relatively well-balanced spatially by eventual sinks/losses (steady-state approximation).
277 Therefore, we can calculate a steady-state lifetime as the ratio between the total burden B (Figure 2c) and the total
278 emissions E or losses L (sum of all emitted / lost molecules, Figure 2a or b) using the following equation: $\tau_{ss} =$
279 B/L (Plumb and Stolarski, 2013).

280
281 We note that the τ_{ss} is more or less the same whether we calculate it using the losses or the emissions. For instance,
282 in selected source regions (rectangles in Figure 2a) the total emissions and losses are very close with very low
283 biases that are less than 2% (not shown here). Our results show that τ_{ss} , on a monthly average, can go up to 12
284 hours, and it can reach 1 day (24 hours) in coastal regions such as region E in New Aquitaine in France. The latter
285 can be related to the high probability of air stagnation is in that area in comparison to Northern Europe (Garrido-
286 Perez et al., 2018), since higher $\text{PM}_{2.5}$ pollution episodes were found under stagnant meteorological conditions
287 (AQEG, 2012); and ammonium molecules carried on these $\text{PM}_{2.5}$ can transform back into ammonia. Our results
288 agree with the literature suggesting a residence time between a few hours to a few days (Behera et al., 2013; Pinder
289 et al., 2008), and with those calculated by Evangeliou et al. (2021) over Europe, showing a monthly average of
290 ammonia lifetime that ranges from 10 to 13 hours in Europe. The figure adapted from Evangeliou et al. (2021) is



291 shown in supplementary material (Figure S1). Shorter lifetimes from industrial sources of ammonia were reported
292 in Damers et al. (2019), with a mean lifetime of ammonia that is equal to 2.35 hours (± 1.16). A recent study
293 found lifetimes of ammonia that vary between 5 and 25 hours, roughly, in Europe (Luo et al., 2022); these values
294 are higher since, in addition to ammonia loss, Luo et al. (2022) included the loss of ammonium, and thus
295 considering the loss of ammonia only terminal when the ammonium is also lost/deposited. This approach is not
296 considered here nor in Evangelidou et al. (2021).

297
298 Notably, ammonia lifetime and burden (Figure 2c, and d) each have different spatial distribution compared to the
299 other 2 panels (Figure 2a, and b). The ammonia residence time in the atmosphere varies depending on the sources
300 and more importantly on the locally dominant loss mechanisms. For this reason, in Figure 3, we show the relative
301 contribution of the ammonia loss mechanisms, presented as pie charts, for the agricultural source regions shown
302 in black boxes in Figure 2a.

303
304 The fastest loss mechanisms are either chemical (i.e. in the vast majority transformation to particulate matter) or
305 through wet and dry deposition (Tournadre et al., 2020). Figure 3 shows that more than 50 % of the ammonia
306 molecules in the atmosphere are lost to chemical reactions in most of the regions (A, B, C, H, and F). The shortest
307 residence time of ammonia is observed in England, where the chemical removal was significantly higher than
308 other sinks and represented up to 73 % of the total ammonia loss pathways, suggesting a rapid transformation into
309 inorganic particulate matter ($PM_{2.5}$). In the regions D, G and E the chemical loss makes up 50 %, 49 %, and 42 %, respectively.
310 In fact, in March 2011, PM was found to be mostly composed of inorganic nitrate (41 %), and ammonium (20 %) (Viatte et al., 2022) over Europe, both of which are products of atmospheric ammonia. Nitrate-bearing $PM_{2.5}$ are formed when nitric acid (HNO_3) reacts with ammonia (Yang et al., 2022), and ammonium is a direct product of the hydrolysis of ammonia. 41% of the nitric acid formed in the atmosphere is produced from the reaction between nitrogen dioxide (NO_2) and the hydroxyl radical (OH) (Alexander et al., 2020). These chemical pathways help explain the large chemical losses in most of the regions studied in Figure 3.

311
312
313
314
315
316
317 Ammonia loss to transport is the highest in regions neighboring the Atlantic Ocean, accounting for 30 %, 27 %, 32 %, and 34 % of total sinks in regions A, D, E, and G respectively. These regions are exposed to the North Atlantic Drift, also known as the Gulf Stream, that is associated with high wind speed and cyclonic activity (Barnes et al., 2022). In other regions, 14 % to 22 % of the total ammonia is lost to transport mechanisms, and in all regions, 11 to 22 % is lost to dry deposition (Figure 3). During March, precipitation is relatively lower as compared to winter (December, January, February) in Europe. Furthermore, 2011 was a particular dry year compared to the 1981 – 2010 average (Met Office, 2016). Drought was reported to be severe in areas such as France, Belgium and the Netherlands, and moderate in England and Ireland (EDO, 2011). This can help explain the low percentage of wet deposition during March 2011 (1 to 5 % out of the total loss of ammonia).

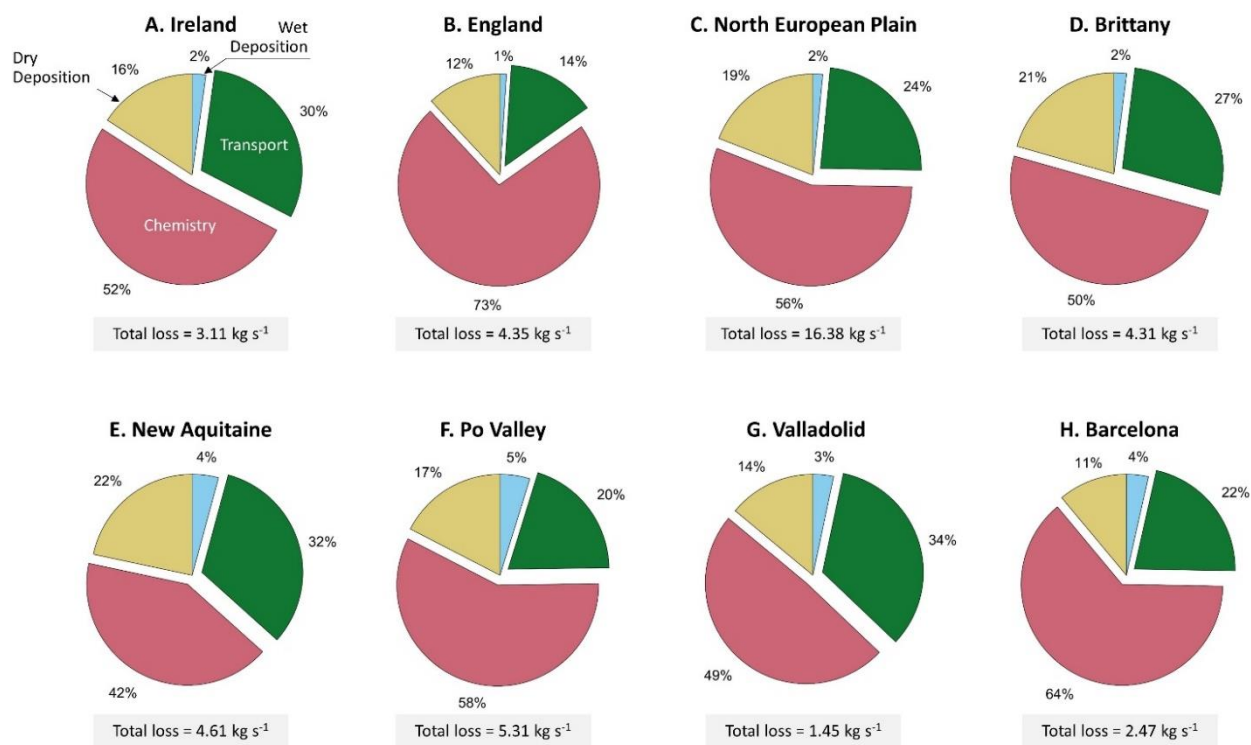


Figure 3. Repartition of the ammonia loss mechanisms for major agricultural areas in Europe, during March 2011, as retrieved from GEOS-Chem, with the total ammonia loss shown in a grey box under each pie chart (kg s⁻¹). The regions are shown in black boxes in Figure 2a.

326

327 4. Ammonia emission potential over Europe

328

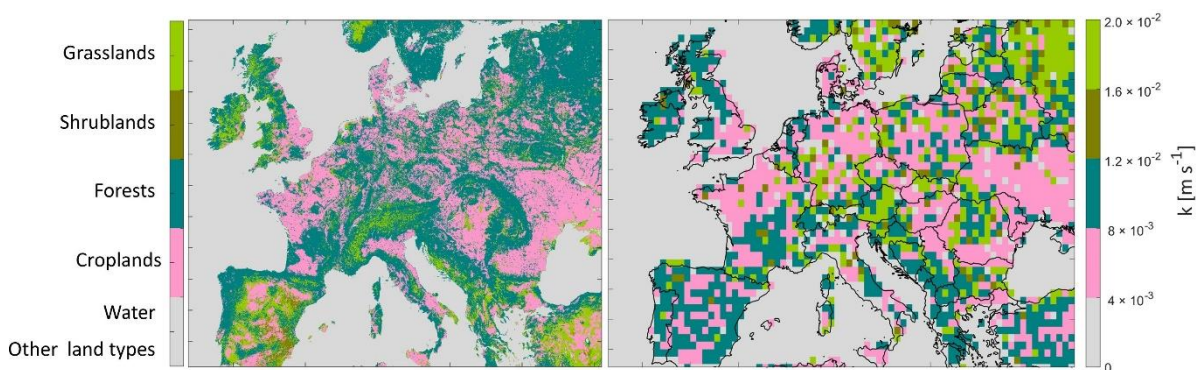
329 To calculate emission potential, a calculation of the mass transfer coefficient k , which relates to the land type, is
 330 necessary. Figure 4 shows the land cover type from MODIS in Europe (left panel), and the corresponding assigned
 331 mass transfer coefficient k (right panel) needed to calculate the emission potential (Eq. (2-1)). In order to choose
 332 a mass transfer coefficient that is convenient for the different land types relevant to this study, we searched for k
 333 values in the literature. Not all land types have been studied for ammonia transfer coefficient.

334 For water bodies and other land types that are not considered here (see Sect. 2.2), the mass transfer values k were
 335 set to zero and represented in grey colour in Figure 4. In a laboratory experiment, Svensson et al. (1993) reported
 336 $k = 4.3 \times 10^{-3} \text{ m s}^{-1}$ for a mixture of soil and swine manure, as therefore, we assign this value to croplands. Due
 337 to the lack of k values for non-fertilized forests, shrublands and grasslands in the literature, we used values
 338 originally assigned for SO₂, bearing in mind that these are approximate values and they reflect mostly the
 339 conditions of the soil cover type (short, medium or tall grass). To assign a k value for forests, we used values
 340 reported in Aneja (1986) ($k = 2 \times 10^{-2} \text{ m s}^{-1}$), which originally represent deposition velocity (mass transfer) of



341 SO₂ in a forest (high crops). For shrublands and grasslands (the two land types have the same k), we used the value
342 $k = 8 \times 10^{-3} \text{ m s}^{-1}$ that has been reported in Aneja et al. (1986) as the deposition velocity (mass transfer) of SO₂
343 in a grassland (medium crops). These values are the best attempt to test the validity of using MODIS and lookup
344 tables of k values to calculate a realistic soil emission potential. As a result, Figure 4 (left panel) includes 5 land
345 types, while k values are reported for 4 land types (other land type/water, croplands, forests, and
346 shrublands/grasslands).

347
348 After choosing the k values, we assigned them for each land type on the (500 m × 500 m) grid. We then extrapolate
349 the array with the k values from 500 m × 500 m to the resolution of GEOS-Chem (0.5° × 0.625° grid box). This
350 leads to averaging different fine pixels with different land cover types into a coarser grid. The result is shown on
351 the right panel of Figure 4.
352



353 **Figure 4. MODIS Land Cover Type, at a 500 m × 500 m grid box (left panel), and interpolated mass transfer coefficient k on a horizontal resolution of 0.5° × 0.625° grid box (right panel).**

354 Uncertainties of this methodological approach can be summarized as follows:

- 355 (1) The k value assigned for croplands is approximate and therefore not the same in every cropland over
356 Europe.
- 357 (2) The k value assigned for forests represents the SO₂ exchange in high croplands, and ammonia might
358 change especially when the latter is highly affected by humidity; it can easily dissolve in the water film
359 on leaves in high humid conditions.
- 360 (3) The extrapolation of a fine array (500 m × 500 m) will merge several grids together and average them in
361 order to construct the coarser grid box (0.5° × 0.625°); the result is therefore an average that might mix
362 croplands with neighboring forests/barelands/grasslands. This leads to a range of different k values that
363 are shown on Figure 4.
364

365 Using the land-type specific k value is necessary in order to reflect realistic emissions potential, as ammonia
366 exchange in a forest is different from that of croplands or unfertilized grasslands, due to different barriers (long,
367 medium or short crop / grass), and ammonium soil content in each land type.

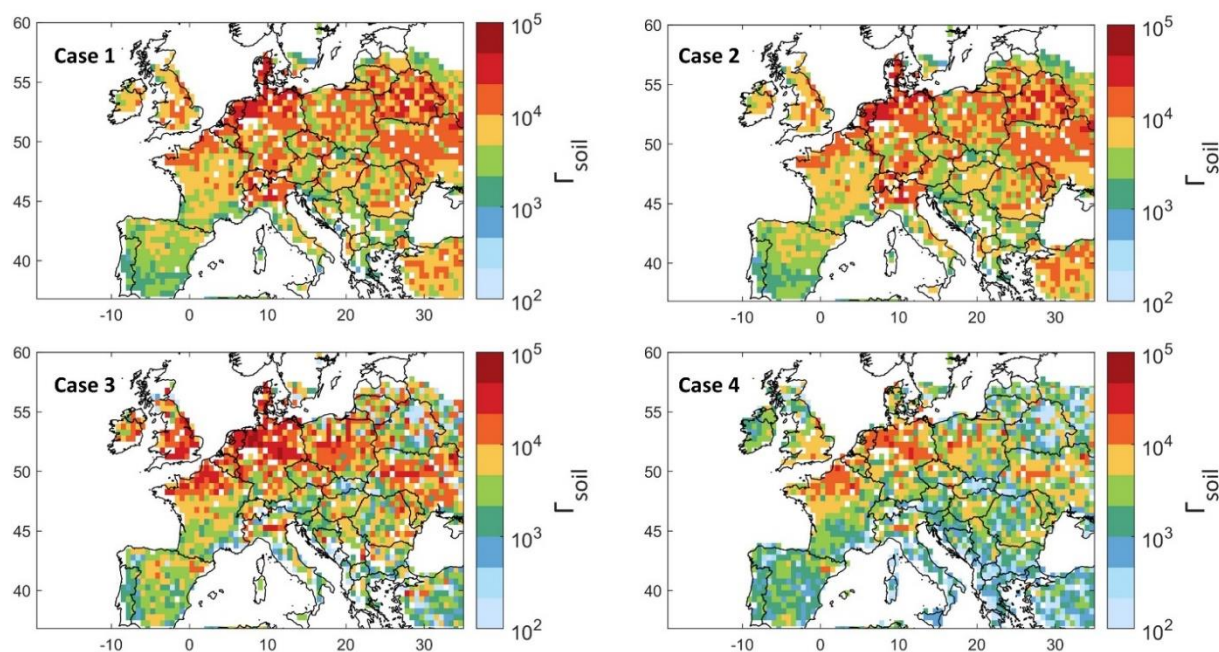


Figure 5. Ammonia soil emission potential (Γ_{soil}) on a log₁₀ scale from model simulation, observation and reanalysis for 4 different cases (see text for details).

368
369 We show in supplementary material Figure S2, the emission potential (similarly to what we show in Figure 5) but
370 from a fixed and averaged k value for all land types. Figure S2 shows the importance of using a variable k that is
371 adjusted to each land type is depicted in supplementary materials (Figure S2). In Figure S2, the fixed k used is
372 calculated assuming 14 days of fertilization ($k = 10^{-3} \text{ m s}^{-1}$), 7 days when k value reduces ($k = 10^{-5} \text{ m s}^{-1}$), and
373 10 days when k is low ($k = 10^{-6} \text{ m s}^{-1}$) resulting in average of $k = 4.5 \times 10^{-4} \text{ m s}^{-1}$. The difference in the
374 emission potential between fixed and spatially variable k is shown in supplementary material Figure S3, where we
375 see that a fixed k might overestimate Γ_{soil} by 10 to 10^3 on a log₁₀ scale (500 – 3000 %), in agricultural areas.

376
377 Figure 5 illustrates the ammonia soil emission potential Γ_{soil} calculated using Eq. (2-1) and k values presented in
378 Figure 4. After assigning the variable mass transfer coefficient, the remaining variables needed to calculate Γ_{soil}
379 in Eq. (2-1) are ammonia concentration and lifetime, as well as the skin temperature. For this reason, the emission
380 potential Γ_{soil} shown in Figure 5 is calculated using different configurations.

- 381
382 - Case 1: GEOS-Chem ammonia and lifetime with MERRA-2 T skin, i.e. simulated Γ_{soil} ,
383 - Case 2: GEOS-Chem ammonia and lifetime and ERA5 Tskin, to check the effect of using ERA5 vs
384 MERRA-2 for skin temperature,
385 - Case 3: IASI ammonia, ERA5 T skin and GEOS-Chem ammonia lifetime,
386 - Case 4: IASI ammonia, ERA5 T skin and ammonia lifetime from Evangeliou et al. (2021), that were
387 calculated using LMDz-OR-INCA chemistry transport model. The latter couples three models: The
388 general circulation model GCM (LMDz) (Hourdin et al., 2006), the INteraction with Chemistry and



389 Aerosols (INCA) (Folberth et al., 2006), and the land surface dynamical vegetation model (ORCHIDEE)
390 (Krinner et al., 2005).

391
392 Based upon the four cases, we calculate a range of emission potentials. When calculating Γ_{soil} , we filtered data
393 points with ammonia total column concentration less than 5×10^{14} molecules cm^{-2} . The latter are mostly grid boxes
394 concentrated above 56° North that we consider as noise (shown in white pixels on Figure 5).
395

396 T skin from ERA5 and MERRA-2 agree very well, with a coefficient of determination $r^2 = 0.97$ (Figure S4 in the
397 supplementary material). This explains the excellent spatial correlation between cases 1 and 2. Since IASI-NH₃
398 retrievals use ERA5 T skin, this also suggests that using MERRA-2 or ERA5 does not affect our Γ_{soil} calculation.
399 In case 3, the emission potential agrees spatially and in value with that of GEOS-Chem. However, we observe
400 higher Γ_{soil} in regions such as Ireland, England, North France, Northeastern Spain, and Poland. This is due to the
401 underestimation/overestimation of ammonia from GEOS-Chem as compared to IASI observations (Figure 1a). For
402 instance, Γ_{soil} from IASI and ERA5 (case 3) differs with that from GEOS-chem and ERA5 (case 2) by up to -70
403 % in the Po Valley (Italy) and +60 % in England. Looking at Table 1, this difference can be explained by the
404 corresponding MRD for each of the regions, in which it is -64 % for England and +110 % for the Po Valley.
405 Similarly, the differences between case 3 and 4 reach up to +66 % in England, and this is mostly due to the 10-
406 hours difference between ammonia lifetime from GEOS-Chem and Evangeliou et al. (2021) (Figure S1 in the
407 supplementary material). The lowest Γ_{soil} were obtained in case 4, due to the higher lifetimes than those calculated
408 from GEOS-Chem (Figure S1); note that Γ_{soil} is inversely proportional to ammonia lifetime (Eq. (2-1)). In fact, the
409 longer ammonia stays in the atmosphere (longer lifetime), the less the flux will be directed from the soil to the
410 atmosphere (less ammonia emission).
411

412 In the four cases presented in Figure 5, we see similar spatial distribution of ammonia emission potential ranging
413 from 12×10^{-1} in a forest to 9.5×10^4 in a cropland (monthly average considering all the cases). In agricultural
414 lands, our results show that Γ_{soil} ranges from 2×10^3 to 9.5×10^4 . Our values for croplands start at around 10^3 . In
415 fact, most of the studies summarized in Zhang et al. (2010) reported Γ_{soil} that range mostly from 10^3 to 10^4 in
416 fertilized croplands/grasslands; the minimum Γ_{soil} reported is in the order of 10^2 and the maximum is of the order
417 of 10^5 . Therefore, our values fit within the range of Γ_{soil} calculated in the literature and summarized in Zhang et
418 al. (2010) and the references within. Personne et al. (2015) focused on Grignon, an agricultural region near Paris,
419 France ($48^\circ 51'N$, $1^\circ 58'E$). They obtained Γ_{soil} values between 1.1×10^4 to 5.8×10^6 . In the present study, the
420 emission potential over this region is between 5×10^3 (case 4) to 2×10^4 (case 2). In this study, it is expected to
421 obtain lower values than the ones measured over specific field. Therefore, we consider our results to be in good
422 agreement with the obtained values in Personne et al. (2015), since ours reflect an average of a coarse patch of
423 land of the size $55 \times 70 \text{ km}^2$ approximately, with a 31-day mean.
424

425 The mean emission potentials per ammonia source region in Europe (shown in rectangles in Figure 2 and Figure
426 3) and per case are shown in Figure 6, and listed in Table 1. Table 1 shows the average lifetime from GEOS-Chem
427 (hours), the average T skin from the three datasets that we used ($^\circ\text{C}$), the average ammonia emission potential in
428 all the cases examined (dimensionless), and the average ammonia columns from IASI and GEOS-Chem
429 (molecules cm^{-2}). The four cases show a similar pattern with the North European Plain exhibiting the highest
430 emission potential. This has been shown in Figure 1, Figure 2, and Figure 5, as well as in Table 1, where Γ_{soil} is
431 higher in regions with high ammonia columns. This is expected in fertilized lands (croplands), since Γ_{soil} is
432 proportional to the concentration of ammonia near the surface. The latter increases when the soil content in
433 ammonium (NH_4^+) increases following the application of nitrogen-based fertilizers.
434



435 Figure 6 also shows that for cases 1 and 2 (GEOS-Chem) the emission potential in the Po Valley is higher as
 436 compared to case 3 (IASI), although it stays within the margin of error. This is due to the effect of temperature.
 437 Table 1 shows that at the time of the IASI overpass, T_{skin} from ERA5 in the Po Valley is almost twice as large
 438 (8.95 °C) as the monthly averaged temperature (4.46 °C). The effect of skin temperature through Eq. (2-1) makes
 439 the emission potential highly dependent. In fact, Γ_{soil} is both directly and inversely proportional to T_{skin} , however,
 440 the exponential in the denominator has ~10 times more effect on the value of Γ_{soil} than the T_{skin} in the numerator.
 441 Therefore, through Eq. (2-1), we conclude that an increase in temperature by 1°C will reduce Γ_{soil} by around -8%.

442
 443 The standard deviation (shaded area) is found to be the highest in the North European Plain, which is also the
 444 largest region (hence higher variability is expected), especially when considering case 3 with IASI. IASI
 445 distinguishes different source sub-regions, leading to higher spatial variability of ammonia, and therefore Γ_{soil} . As
 446 Figure 5 has shown, case 4 has the lowest Γ_{soil} , with a factor of two lower than cases 1 to 3. This is due to the
 447 longer lifetimes calculated by Evangeliou et al. (2021). However, we note that all the regions exhibit the same
 448 inter-variability between each of the case, regardless of the lifetimes used.
 449

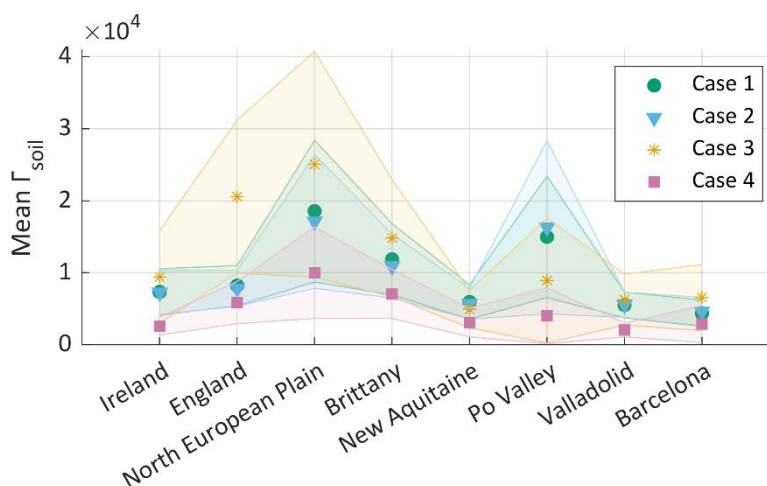


Figure 6. Mean ammonia emission potential Γ_{soil} per region and per case, with the error margin on the mean as the shaded area (95th percentile) for cases 1 to 4. The cases are explained in Figure 5 and its discussion.

450
 451
 452
 453
 454
 455
 456
 457
 458
 459
 460



461 **Table 1.** Summary of NH₃ average lifetime, emission potential, concentrations and the T skin in selected regions
 462 in Europe.

463

Region	Country	τ_{NH_3} [hours]	T skin [°C]			$\Gamma_{soil} \times 10^4$ [dimensionless]				NH ₃ concentrations [molecules $\times 10^{15}$ cm ⁻²]		
			ERA5 IASI Overpass	ERA5	MERRA- 2	Case 1	Case 2	Case 3	Case 4	IASI	GEOS- Chem	Mean MRD [%]
Ireland	Ireland	3.34	8.74	5.78	6.23	0.73	0.72	0.94	0.26	2.5	1.5	- 46
England	England	3.15	8.54	5.87	5.73	0.82	0.78	2.06	0.58	4.8	1.2	- 64
North European Plains	Belgium, Netherlands	5.16	7.46	4.93	4.57	1.86	1.71	2.51	1.00	7.7	3.9	- 49
Brittany	France	6.93	10.48	8.13	8.16	1.19	1.09	1.48	0.70	5.8	3.7	- 60
New Aquitaine	France	8.05	11.25	7.72	7.47	0.59	0.57	0.49	0.30	4.0	2.9	- 20
Po Valley	Italy	7.10	8.95	4.46	5.46	1.50	1.63	0.89	0.40	3.8	4.0	+ 110
Valladolid	Spain	4.53	11.64	6.87	6.93	0.55	0.55	0.62	0.20	2.5	1.3	- 42
Barcelona	Spain	4.94	12.61	7.05	9.44	0.43	0.46	0.65	0.28	3.2	1.5	- 49



464 5. Ammonia under future scenarios

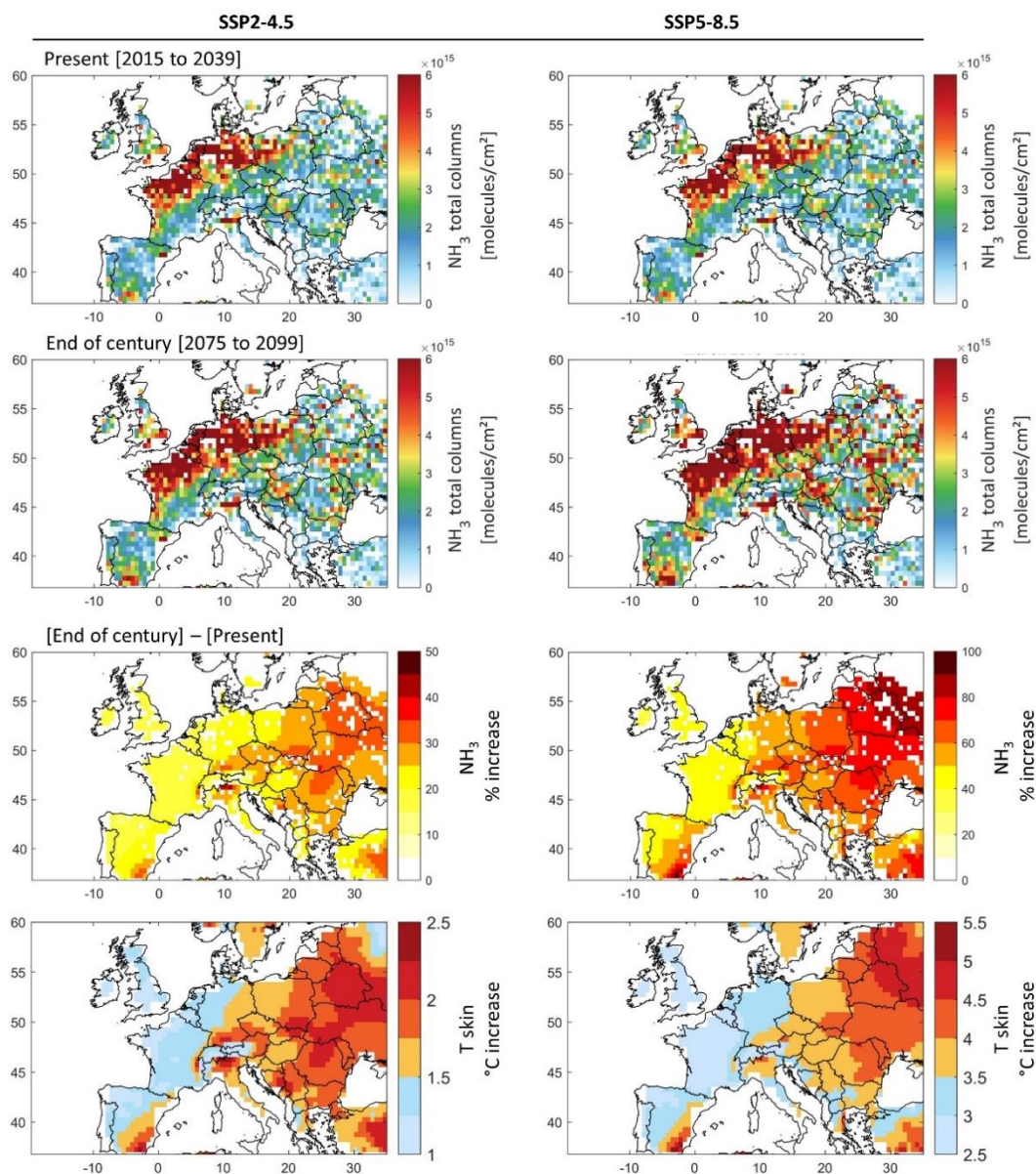


Figure 7. First and second rows: Ammonia total column concentrations during March (monthly averages) under the present climate [2015 to 2039] (first row), and in the end of century climate [2075 to 2099] (second row), under the socio-economic scenarios SSP2-4.5 (left) and SSP5-8.5 (right). Third and fourth rows: The percentage increase in ammonia concentration (third row), and the change in T skin in °C (fourth row) by the end of the century [2075 to 2099] with respect to present climate [2015 to 2039] under SSP2-4.5 (left) and SSP5-8.5 (right). Ammonia columns were calculated using ammonia emission potential Γ_{soil} derived from IASI and ERA5 for March 2011 (case 3), and EC-Earth T skin simulations for SSP2-4.5 and SSP5-8.5 extending from 2015 till 2099.



465 As seen in Eq. (2-1), higher skin temperatures favour volatilization of ammonia from the soil. In an attempt to
466 understand how our simplified emission potential model behaves under changing climate, as well as under future
467 scenarios, we adopt the future T skin simulations from EC-Earth climate model, into Eq. (2-1). The two climate
468 socio-economic scenarios that we consider are SSP2-4.5 (“middle of the road” scenario where trends broadly
469 follow their historical patterns), and SSP5-8.5 (a world of rapid and unconstrained growth in economic output and
470 energy use) (Riahi et al., 2017). The same Figure constructed using Γ_{soil} from GEOS-Chem (case 1) is shown in
471 the supplementary material as Figure S5.

472 We calculate current and future ammonia columns assuming that the emission potential Γ_{soil} remains unchanged.
473 In other words, we assume that the same amount of fertilizers and manure is used until 2100 in the agricultural
474 fields and farms (unchanged ammonium soil content).

475 Figure 7 shows ammonia columns during the 25-year [2015 – 2039] representing the present climate (upper
476 panels), and the end of the century [2075 – 2099] (middle panels). The ammonia columns in the 25-year average
477 climate of the end of century with respect to present day climate (lower panels) are also shown.

478
479 Spatially, the present climate ammonia columns calculated from the T skin of the climate model and our emission
480 potential from IASI (case 3 in Figure 5), agree very well with those shown in Figure 1. We do not aim at validating
481 or directly comparing the two, as we are only interested in the climate response on ammonia concentration, i.e. by
482 the difference due to skin temperature increase (lower panels).

483
484 From Figure 7 (lower panels) it can be seen that the increase in ammonia columns by the end of the century is
485 more severe on the east side of Europe. Under the most likely scenario (SSP2-4.5), ammonia columns vary between
486 +15 % in France, to around +20 % in the North European Plain (Figure 7). The largest increase is detected in
487 Eastern Europe, where ammonia columns show an increase of up to a +50 % (Figure 7, lower left panels), creating
488 new potential hotspots/sources of ammonia in Belarus, Ukraine, Hungary, Moldova, parts of Romania and
489 Switzerland. Under the SSP5-8.5 scenario, the results show an increase in ammonia columns of up to +100 % in
490 Eastern Europe (Figure 7, right lower panel). This is directly related to the higher projected increase in skin
491 temperature over these regions. Other studies have equally reported Eastern Europe to be more affected by climate
492 change under future scenarios, as compared to western Europe (European Environment Agency, 2022; Jacob et al.,
493 2018). Spatially, the increase in ammonia coincides with the increase in T skin.

494 Figure 8 depicts the change in ammonia columns under the SSP2-4.5 and SSP5-8.5 scenarios, for our source
495 regions (shown as rectangles in Figure 2). Ammonia columns increase is foreseen to be the highest in the Po Valley
496 (Italy) with +26 % and +59 % under SSP2-4.5 and SSP5-8.5 respectively. It is then followed by the agricultural

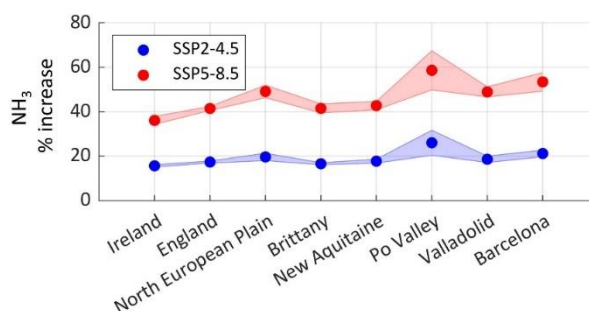


Figure 8. The percentage increase in ammonia concentration by the end of the century [2075 to 2099] with respect to the present climate [2015 to 2039] under the two climate scenarios SSP2-4.5 (blue) and SSP5-8.5 (red), in the source regions investigated in this study. The shades around each line represent the standard deviation from the mean.



497 areas around Barcelona (Spain), and the North European Plain (Belgium, Netherlands) with an increase of +21 %
498 (+49 %) and +20 % (+53 %) respectively, under the SSP2-4.5 (SSP5-8.5) scenario. Under the SSP5-8.5, the
499 increase in ammonia columns in percentage is more than twice the change under SSP2-4.5 (+127 % in the case of
500 the Po Valley for instance). The Po Valley is adjacent to the Alps mountains, and due to global warming, this
501 region is expected to experience increased evapotranspiration (Donnelly et al., 2017), which is a major factor that
502 leads to the volatilization of ammonia.

503 The local and regional effect of volatilization of ammonia under different climate scenarios remains difficult to be
504 properly assessed. Even under the “middle of the road” scenario 2-4.5, and without climate extremes (e.g.
505 heatwaves), Europe might be facing big challenges in air or downwind agricultural regions, since chemistry and
506 atmospheric transport (Figure 3) drive the loss of ammonia during the growing season in this part of the world.

507
508 An increase in ammonia concentration poses a significant and yet poorly understood effect on local and regional
509 air quality through the increase in $PM_{2.5}$ concentration. We note, however, that ammonia columns in the soil are
510 governed by a threshold. Higher temperatures will increase the rate of volatilization of ammonia from the soil, but
511 only up to a certain point where no dissolved ammonium is left. Plants, however, can also be a source of ammonia
512 when exposed to stressful conditions. For example, under heat stress and in instances where there are no ammonia
513 in the air, increase in air temperature results in exponential increase in ammonia emission from plants’ leaves
514 (Husted and Schjoerring, 1996).

515 6. Discussion and conclusions

516
517 Agriculture worldwide has fed the human race for thousands of years, and will continue to do so, as mankind
518 highly relies on it. Emissions from agricultural activities will inevitably increase, in order to meet the expected
519 yield. In this study, we use a variety of state-of-the-art datasets (satellite, reanalysis and model simulation) to
520 calculate the first regional map of ammonia emission potential during the start of the growing season in Europe.
521 The emission potential can be used as a proxy to calculate ammonia columns in the atmosphere, and as such to
522 assess its deposition, atmospheric transport, and contribution to PM formation. First, we show that the GEOS-
523 Chem chemistry transport model is able to reproduce key spatio-temporal patterns of ammonia levels over Europe.
524 The ammonia budget is governed by the emissions over source regions (North European Plain, Brittany and the
525 Po valley), as well as by key loss processes. We find that chemical loss pathway is responsible of 50 % or more of
526 the total ammonia loss over Europe. From the GEOS-Chem simulation, we calculate the average ammonia lifetime
527 in the atmosphere which ranges between 4 and 12 hours in agricultural source regions of Europe. From this, and
528 using the mass transfer coefficient for different land cover types, we calculate a range of emission potentials
529 Γ_{soil} from IASI and GEOS-Chem. We find that Γ_{soil} ranges between from 2×10^3 to 9.5×10^4 in fertilized lands
530 (croplands). Choosing a variable k from the literature, and based on different land cover types from MODIS, we
531 calculate Γ_{soil} values that are consistent with those found in the literature. The increase in T skin is expected to
532 have an effect on the emission of ammonia from the soil. Using T skin from the EC-Earth climate model, we
533 estimate ammonia columns by the end of the century [2075 – 2099], and compare it to columns of the present
534 climate [2015 – 2039]. Our results show that ammonia columns will double under the SSP5-8.5 scenario, and will
535 increase by up to 50 % under the most likely SSP2-4.5 scenario. The eastern part of Europe is the most affected
536 by the change in temperatures, and it is where we find the highest ammonia columns increase. Among the regions
537 of focus, Italy, Spain, Belgium and the Netherlands are the most affected, as compared to France, England and
538 Ireland. The highest increase in ammonia columns is observed in the Po Valley in Italy (+59 % under the SSP5-
539 8.5).

540



541 We calculate ammonia concentration under future climate and during the start of the growing season (March) in
542 Europe. However, in order to grasp the yearly budget of ammonia, it is crucial to apply this method to all seasons
543 of the year; especially in regions with extensive agricultural activities, such as the United States, India, and China.
544 In addition to this, more field measurements of ammonia emission potential (I_{soil}) in different land use / cover
545 types are required, this can help us perform better comparison with emission potentials calculated from model and
546 satellite data. Finally, having ammonia columns at different times of the day, from field observations or satellite
547 measurements will allow quantification of daily emission potentials, that will in turn help us understand its diurnal
548 variability. This will be ensured with the launch of the Infrared Sounder (IRS) on the Meteosat Third Generation
549 (MTG) geostationary satellites scheduled in 2025.



550
 551

A. Appendix A

552 1. Ammonia-Ammonium equilibrium

553 Ammonia (NH_3) is a water-soluble gas, it undergoes protonation with H^+ from the hydronium ion H_3O^+ in an
 554 aqueous solution in order to give ammonium (NH_4^+ cation), the dissociation equation is expressed as follows:



555
 556

Or



557
 558

With $K_{NH_4^+}$ as the ammonium-ammonia dissociation equilibrium constant that can be expressed as:

$$K_{NH_4^+} = \frac{[NH_{3(aq)}][H^+]}{[NH_4^+(aq)]} \quad (A-3)$$

559
 560

561 The solubility of ammonia in water is affected by the temperature and the acidity (pH) of the solvent (water). The
 562 equilibrium constant can be expressed as follows:

$$K_{NH_4^+} = 5.67 \cdot 10^{-10} \exp \left[-6286 \left(\frac{1}{T} - \frac{1}{298.15} \right) \right] \quad (A-4)$$

563

564 2. Henry's equilibrium

565 Upon its dissolution in water, NH_3 obeys the Henry's law. Ammonia gas ($NH_{3(g)}$) near the surface of the solvent
 566 is in equilibrium with the dissolved ammonia in the aqueous phase $NH_{3(aq)}$ (in water). Henry's equilibrium is
 567 expressed as follows:



568
 569

With H_{NH_3} as the Henry's constant, it can be expressed as follows (Wichink Kruit, 2010):

$$H_{NH_3} = \frac{[NH_{3(aq)}]}{[NH_{3(g)}]} = 5.527 \cdot 10^{-4} \cdot \exp \left[4092 \left(\frac{1}{T} - \frac{1}{298.15} \right) \right] \quad (A-6)$$

570
 571

The partial pressure of ammonia near the surface of the soil can be calculated using Henry's constant and the
 572 dissociation equilibrium (Wichink Kruit, 2010):

$$P_{NH_3} = \frac{K_{NH_4^+} [NH_4^+]}{H_{NH_3} [H^+]} = \frac{5.67 \cdot 10^{-10} \cdot \exp \left[-6286 \left(\frac{1}{T} - \frac{1}{298.15} \right) \right]}{5.527 \cdot 10^{-4} \cdot \exp \left[4092 \left(\frac{1}{T} - \frac{1}{298.15} \right) \right]} \times \frac{[NH_4^+]}{[H^+]} \quad (A-7)$$

573
 574
 575

If we use the ideal gas law ($PV=nRT$), we can draw the link between the mass density of ammonia ($NH_{3(g)}$) and
 the partial pressure:



$$\chi_{NH_3} = \frac{P_{NH_3} \cdot M_{NH_3}}{R \cdot T} \quad (\text{A-8})$$

576
 577 Where χ_{NH_3} is the concentration of NH_3 at the soil surface ($kg\ m^{-3}$), P_{NH_3} is the partial pressure of NH_3 near the
 578 surface (atm), M_{NH_3} is the molar mass of NH_3 ($kg\ mol^{-1}$), R is the gas constant ($0.082\ atm\ L\ mol^{-1}\ K^{-1}$), and T is
 579 the temperature in Kelvin.

580 Substituting Eq. (A-5) in (A-6) we get:

$$\chi_{NH_3} = \frac{2.75 \cdot 10^9 \left(\frac{gK}{m^3}\right)}{T_{soil}} \exp\left[\frac{-1.04 \cdot 10^4}{T_{soil}}\right] \Gamma_{soil} \quad (\text{A-9})$$

581
 582 Where χ_{NH_3} is the concentration of ammonia at the soil surface at equilibrium ($g\ m^{-3}$), and is referred to as the
 583 compensation point, T_{soil} is the temperature of the soil (Kelvin), Γ_{NH_3} is the NH_3 emission potential from the soil
 584 and is a dimensionless ratio between $[NH_4^+]$ and $[H^+]$.

585 3. Ammonia total columns from IASI

586 In this study we use the total columns of ammonia from IASI (molecules m^{-2}) in order to calculate the emission
 587 potential Γ_{soil} , we should draw the link between these columns and this parameter. The bi-directional exchange of
 588 NH_3 between the surface and the atmosphere can be expressed by the flux (assuming a flux independent of time)
 589 (Roelle and Aneja, 2005; Zhang et al., 2010):

$$Flux_{NH_3} = k ([NH_3]^{soil} - [NH_3]^{atm}) \quad (\text{A-10})$$

590
 591 Where $Flux_{NH_3}$ is the bidirectional flux between the soil and the atmosphere (molecules ($m^2\ s^{-1}$)), k is the soil –
 592 atmosphere exchange velocity ($m\ s^{-1}$), also known as the mass transfer coefficient; $[NH_3]^{soil}$ is the concentration
 593 of $NH_{3(g)}$ in the soil, and $[NH_3]^{atm}$ is the concentration of $NH_{3(g)}$ in the atmosphere (molecules m^{-3}).
 594 Assuming a first order dissociation of NH_3 , we can express the change in the $[NH_3]^{col}$ total columns as follows:

$$\frac{d [NH_3]^{col}}{dt} = Flux_{NH_3} - k' [NH_3]^{col} \quad (\text{A-11})$$

595
 596 Where k' is the rate of dissociation of first order $k' = 1/\tau$ ($m\ s^{-1}$), with τ the lifetime of NH_3 in the atmosphere.
 597 Assuming steady state, and considering the $[NH_3]^{atm}$ as the $[NH_3]^{col}$, and $[NH_3]^{soil}$ as χ_{NH_3} , Eq. (A-9) can be
 598 written as:

$$k \left(\frac{N_a \cdot \chi_{NH_3}}{M_{NH_3}} - \frac{1}{c} [NH_3]^{col} \right) = \frac{[NH_3]^{col}}{\tau} \quad (\text{A-12})$$

599
 600 Where c is the column height and is equal to 6 km. It is important to note that we neglect the effect of transport by
 601 wind since we only look at large regions. Finally, the total column of ammonia $[NH_3]^{col}$ can be written as:

$$[NH_3]^{col} = \frac{N_a \cdot \chi_{NH_3}}{M_{NH_3} \cdot \left(c + \frac{1}{k\tau}\right)} \quad (\text{A-13})$$

602
 603 The column height is not considered anymore because it is negligible compared to $1/k\tau$, using Eq. (A-6) in (A-
 604 11) we get:



$$[NH_3]^{col} = \frac{2.75 \cdot 10^{27} \left(\frac{gK}{cm^3}\right)}{T_{soil}} \exp\left[\frac{-1.04 \cdot 10^4}{T_{soil}}\right] \Gamma_{NH_3} \cdot k\tau \quad \left(\frac{molecules}{cm^2}\right) \quad (A-14)$$

605

606 Note that $2.75 \cdot 10^{27} = \frac{a \cdot N_a \cdot c'}{M_{NH_3}} \left(\frac{K \text{ molecules}}{cm^3}\right)$, where $a = 2.75 \cdot 10^3 \text{ (g K cm}^{-3}\text{)}$, N_a Avogadro's number
607 ($6.0221409 \times 10^{23} \text{ molecules mol}^{-1}$), 10^{-2} is added to convert k from $m \text{ s}^{-1}$ to $cm \text{ s}^{-1}$, and M_{NH_3} the molar mass of
608 NH_3 ($17.031 \text{ g mol}^{-1}$). The emission potential of NH_3 from the soil can we written as:

$$\Gamma_{soil} = \frac{[NH_3]^{col} \cdot T_{soil}}{\exp\left(\frac{-b}{T_{soil}}\right)} \frac{M_{NH_3}}{a \cdot N_a \cdot 10^{-2}} \cdot \frac{1}{k\tau} \quad (A-15)$$

609

610 Where $b = 1.04 \times 10^4 \text{ K}$.



611 Author contribution

612 RA contributed to the conception and design of the article, developed the code, wrote the manuscript, analysed and
613 interpreted of the data, and approved the version for submission; CV, CC, and PFC revised the manuscript; WCP provided
614 the GEOS-Chem simulation data, and revised the manuscript; NE provided ammonia lifetime calculation using the LMDz-
615 OR-INCA chemistry transport model and commented on the manuscript; MVD and LC contributed to the acquisition of the
616 IASI ammonia data (NH₃-v3R-ERA5), and revised the manuscript; SS contributed to the conception and design of the article,
617 provided the EC-Earth temperature data, and revised the manuscript, and approved the version for submission.

618 Acknowledgments

619 The IASI mission is a joint mission of Eumetsat and the Centre National d'Etudes Spatiales (CNES, France). The authors
620 acknowledge the AERIS data infrastructure for providing the IASI L1C and L2 data.

621 Funding information

622 Rimal Abeed is grateful to CNES for financial support. The research in Belgium was funded by the Belgian State Federal
623 Office for Scientific, Technical and Cultural Affairs (Prodex HIRS) and the Air Liquide Foundation (TAPIR project). This
624 work is also partly supported by the FED-tWIN project ARENBERG ("Assessing the Reactive Nitrogen Budget and Emissions
625 at Regional and Global Scales") funded via the Belgian Science Policy Office (BELSPO). L. Clarisse is Research Associate
626 supported by the Belgian F.R.S.-FNRS. C. Clerbaux is grateful to CNES for scientific collaboration and financial support. N.
627 Evangeliou was funded by Norges Forskningsråd (ROM- FORSK – Program for romforskning of the Research Council of
628 Norway (grant no. 275407)).

629 Competing interests

630 The authors are aware of no competing interests.

631 Data accessibility statement

632 The IASI-NH₃ used in this study are retrieved from the AERIS data infrastructure (<https://iasi.aeris-data.fr/nh3r-era5/>). ERA5
633 skin temperature from 1979 to present are available for download in the following DOI: [10.24381/cds.adbb2d47](https://doi.org/10.24381/cds.adbb2d47). The GEOS-
634 Chem outputs used in this study are only available upon request. EC-Earth3 model output prepared for CMIP6 ScenarioMIP
635 are retrieved here: <https://doi.org/10.22033/ESGF/CMIP6.727>. The MODIS land cover data are available for download in the
636 following link: <https://doi.org/10.5067/MODIS/MCD12Q1.006>.

637
638
639
640
641
642
643
644
645



646 References

- 647 Abeer, R., Clerbaux, C., Clarisse, L., Van Damme, M., Coheur, P.-F., and Safieddine, S. A space view of agricultural and
648 industrial changes during the Syrian civil war. *Elem. Sci. Anthr.* <https://doi.org/10.1525/elementa.2021.000041>
649 (2021)
- 650 Adams, C., McLinden, C. A., Shephard, M. W., Dickson, N., Dammers, E., Chen, J., Makar, P., Cady-Pereira, K. E., Tam,
651 N., Kharol, S. K., Lamsal, L. N., and Krotkov, N. A. Satellite-derived emissions of carbon monoxide, ammonia, and
652 nitrogen dioxide from the 2016 Horse River wildfire in the Fort McMurray area. *Atmospheric Chem. Phys.*
653 <https://doi.org/10.5194/acp-19-2577-2019> (2019)
- 654 Alexander, B., Sherwen, T., Holmes, C. D., Fisher, J. A., Chen, Q., Evans, M. J., and Kasibhatla, P. Global inorganic nitrate
655 production mechanisms: Comparison of a global model with nitrate isotope observations. *Atmospheric Chem. Phys.*
656 <https://doi.org/10.5194/acp-20-3859-2020> (2020)
- 657 Aneja, V. P., Rogers, H. H., and Stahel, E. P. Dry Deposition of Ammonia at Environmental Concentrations on Selected
658 Plant Species. *J. Air Pollut. Control Assoc.* <https://doi.org/10.1080/00022470.1986.10466183> (1986)
- 659 AQEG. *Fine particulate matter (PM_{2.5}) in the United Kingdom* (p. 203). Air Quality Expert Group (AQEG), prepared for
660 the Department for Environment, Food and Rural Affairs (Defra), Scottish Executive, Welsh Government and the
661 Department of the Environment in Northern Ireland. [https://uk-
662 air.defra.gov.uk/assets/documents/reports/cat11/1212141150 AQEG Fine Particulate Matter in the UK.pdf](https://uk-air.defra.gov.uk/assets/documents/reports/cat11/1212141150_AQEG_Fine_Part particulate_Matter_in_the_UK.pdf)
663 (2012)
- 664 Barnes, A. P., Svensson, C., and Kjeldsen, T. R. North Atlantic air pressure and temperature conditions associated with
665 heavy rainfall in Great Britain. *Int. J. Climatol.* <https://doi.org/10.1002/joc.7414> (2022)
- 666 Bauer, S. E., Tsigaridis, K., and Miller, R. Significant atmospheric aerosol pollution caused by world food cultivation.
667 *Geophys. Res. Lett.* <https://doi.org/10.1002/2016GL068354> (2016)
- 668 Behera, S. N., Sharma, M., Aneja, V. P., and Balasubramanian, R. Ammonia in the atmosphere: A review on emission
669 sources, atmospheric chemistry and deposition on terrestrial bodies. *Env. Sci Pollut Res.*
670 <https://doi.org/10.1007/s11356-013-2051-9> (2013)
- 671 Belward, A. S., Estes, John E., and Kline, K. D. The IGBP-DIS Global 1-Km Land-Cover Data Set DIS-Cover: A Project
672 Overview. *Photogramm. Eng. Remote Sens.* [https://www.asprs.org/wp-
673 content/uploads/pers/1999journal/sep/1999_sept_1013-1020.pdf](https://www.asprs.org/wp-content/uploads/pers/1999journal/sep/1999_sept_1013-1020.pdf) (1999)
- 674 Bey, I., Jacob, D. J., Yantosca, R. M., Logan, J. A., Field, B. D., Fiore, A. M., Li, Q., Liu, H. Y., Mickley, L. J., and Schultz,
675 M. G. Global modeling of tropospheric chemistry with assimilated meteorology: Model description and evaluation.
676 *J. Geophys. Res. Atmospheres.* <https://doi.org/10.1029/2001JD000807> (2001)
- 677 Bouwman, A. F., Lee, D. S., Asman, W. a. H., Dentener, F. J., Van Der Hoek, K. W., and Olivier, J. G. J. A global high-
678 resolution emission inventory for ammonia. *Glob. Biogeochem. Cycles.* <https://doi.org/10.1029/97GB02266> (1997)
- 679 Clarisse, L., Van Damme, M., Clerbaux, C., and Coheur, P.-F. Tracking down global NH₃ point sources with wind-adjusted
680 superresolution. *Atmospheric Meas. Tech.* <https://doi.org/10.5194/amt-12-5457-2019> (2019)
- 681 Clarisse, L., Van Damme, M., Gardner, W., Coheur, P.-F., Clerbaux, C., Whitburn, S., Hadji-Lazaro, J., and Hurtmans, D.
682 Atmospheric ammonia (NH₃) emanations from Lake Natron's saline mudflats. *Sci. Rep.*
683 <https://doi.org/10.1038/s41598-019-39935-3> (2019)
- 684 Clerbaux, C., Boynard, A., Clarisse, L., George, M., Hadji-Lazaro, J., Herbin, H., Hurtmans, D., Pommier, M., Razavi, A.,
685 Turquety, S., and Wespes, C. Monitoring of atmospheric composition using the thermal infrared IASI/MetOp
686 sounder. *Atmospheric Chem. Phys.* <https://doi.org/10.5194/acp-9-6041-2009> (2009)
- 687 Coheur, P.-F., Clarisse, L., Turquety, S., Hurtmans, D., and Clerbaux, C. IASI measurements of reactive trace species in
688 biomass burning plumes. *Atmospheric Chem. Phys.* <https://doi.org/10.5194/acp-9-5655-2009> (2009)
- 689 Dammers, E., McLinden, C. A., Griffin, D., Shephard, M. W., Van Der Graaf, S., Lutsch, E., Schaap, M., Gainairu-Matz, Y.,
690 Fioletov, V., Van Damme, M., Whitburn, S., Clarisse, L., Cady-Pereira, K., Clerbaux, C., Coheur, P. F., and
691 Erismann, J. W. NH₃ emissions from large point sources derived from CrIS and IASI satellite observations.
692 *Atmospheric Chem. Phys.* <https://doi.org/10.5194/acp-19-12261-2019> (2019)



- 693 David, M., Loubet, B., Cellier, P., Mattsson, M., Schjoerring, J. K., Nemitz, E., Roche, R., Riedo, M., and Sutton, M. A.
694 Ammonia sources and sinks in an intensively managed grassland canopy. *Biogeosciences*.
695 <https://doi.org/10.5194/bg-6-1903-2009> (2009)
- 696 Donnelly, C., Greuell, W., Andersson, J., Gerten, D., Pisacane, G., Roudier, P., and Ludwig, F. Impacts of climate change on
697 European hydrology at 1.5, 2 and 3 degrees mean global warming above preindustrial level. *Clim. Change*.
698 <https://doi.org/10.1007/s10584-017-1971-7> (2017)
- 699 Döscher, R., Acosta, M., Alessandri, A., Anthoni, P., Arneth, A., Arsouze, T., Bergmann, T., Bernadello, R., Boussetta, S.,
700 Caron, L.-P., Carver, G., Castrillo, M., Catalano, F., Cvijanovic, I., Davini, P., Dekker, E., Doblas-Reyes, F. J.,
701 Docquier, D., Echevarria, P., ... Zhang, Q. The EC-Earth3 Earth System Model for the Climate Model
702 Intercomparison Project 6. *Geosci. Model Dev. Discuss.* <https://doi.org/10.5194/gmd-2020-446> (2021)
- 703 ECMWF. *IFS Documentation CY43R1*. ECMWF. <https://www.ecmwf.int/sites/default/files/elibrary/2016/17117-part-iv-physical-processes.pdf> (2016)
- 704
705 EDO, G. D. O. *Drought news in Europe: Situation in April 2011—Short Analysis of data from the European Drought
706 Observatory (EDO)* (p. 2). <https://edo.jrc.ec.europa.eu/documents/news/EDODroughtNews201104.pdf> (2011)
- 707 Erisman, J. W., Van Pul, A., and Wyers, P. Parametrization of surface resistance for the quantification of atmospheric
708 deposition of acidifying pollutants and ozone. *Atmos. Environ.* [https://doi.org/10.1016/1352-2310\(94\)90433-2](https://doi.org/10.1016/1352-2310(94)90433-2)
709 (1994)
- 710 European Environment Agency. *Global and European temperatures*. <https://www.eea.europa.eu/ims/global-and-european-temperatures> (2022)
- 711
712 Evangelizou, N., Balkanski, Y., Eckhardt, S., Cozic, A., Van Damme, M., Coheur, P.-F., Clarisse, L., Shephard, M., Cady-
713 Pereira, K., and Hauglustaine, D. 10-year satellite-constrained fluxes of ammonia improve performance of
714 chemistry transport models. *Atmospheric Chem. Phys.* <https://doi.org/10.5194/acp-21-4431-2021> (2021)
- 715 Eyring, V., Bony, S., Meehl, G. A., Senior, C. A., Stevens, B., Stouffer, R. J., and Taylor, K. E. Overview of the Coupled
716 Model Intercomparison Project Phase 6 (CMIP6) experimental design and organization. *Geosci. Model Dev.*
717 <https://doi.org/10.5194/gmd-9-1937-2016> (2016)
- 718 FAO. *FAO, GIEWS, Earth Observation*.
719 <https://www.fao.org/giews/earthobservation/country/index.jsp?lang=en&code=FRA> (2022)
- 720 Flechard, C. R., Massad, R.-S., Loubet, B., Personne, E., Simpson, D., Bash, J. O., Cooter, E. J., Nemitz, E., and Sutton, M.
721 A. Advances in understanding, models and parameterizations of biosphere-atmosphere ammonia exchange.
722 *Biogeosciences*. <https://doi.org/10.5194/bg-10-5183-2013> (2013)
- 723 Flechard, C. R., Nemitz, E., Smith, R. I., Fowler, D., Vermeulen, A. T., Bleeker, A., Erisman, J. W., Simpson, D., Zhang, L.,
724 Tang, Y. S., and Sutton, M. A. Dry deposition of reactive nitrogen to European ecosystems: A comparison of
725 inferential models across the NitroEurope network. *Atmospheric Chem. Phys.* <https://doi.org/10.5194/acp-11-2703-2011> (2011)
- 726
727 Flechard, C. R., Spirig, C., Neftel, A., and Ammann, C. The annual ammonia budget of fertilised cut grassland – Part 2:
728 Seasonal variations and compensation point modeling. *Biogeosciences*. <https://doi.org/10.5194/bg-7-537-2010>
729 (2010)
- 730 Folberth, G. A., Hauglustaine, D. A., Lathière, J., and Brocheton, F. Interactive chemistry in the Laboratoire de Météorologie
731 Dynamique general circulation model: Model description and impact analysis of biogenic hydrocarbons on
732 tropospheric chemistry. *Atmospheric Chem. Phys.* <https://doi.org/10.5194/acp-6-2273-2006> (2006)
- 733 Garrido-Perez, J. M., Ordóñez, C., García-Herrera, R., and Barriopedro, D. Air stagnation in Europe: Spatiotemporal
734 variability and impact on air quality. *Sci. Total Environ.* <https://doi.org/10.1016/j.scitotenv.2018.07.238> (2018)
- 735 Gelaro, R., McCarty, W., Suárez, M. J., Todling, R., Molod, A., Takacs, L., Randles, C. A., Darmenov, A., Bosilovich, M.
736 G., Reichle, R., Wargan, K., Coy, L., Cullather, R., Draper, C., Akella, S., Buchard, V., Conaty, A., Silva, A. M. da,
737 Gu, W., ... Zhao, B. The Modern-Era Retrospective Analysis for Research and Applications, Version 2 (MERRA-
738 2). *J. Clim.* <https://doi.org/10.1175/JCLI-D-16-0758.1> (2017)
- 739 Hersbach, H., Bell, B., Berrisford, P., Hirahara, S., Horányi, A., Muñoz-Sabater, J., Nicolas, J., Peubey, C., Radu, R.,
740 Schepers, D., Simmons, A., Soci, C., Abdalla, S., Abellan, X., Balsamo, G., Bechtold, P., Biavati, G., Bidlot, J.,
741 Bonavita, M., ... Thépaut, J.-N. The ERA5 global reanalysis. *Q. J. R. Meteorol. Soc.*
742 <https://doi.org/10.1002/qj.3803> (2020)



- 743 Hoesly, R. M., Smith, S. J., Feng, L., Klimont, Z., Janssens-Maenhout, G., Pitkanen, T., Seibert, J. J., Vu, L., Andres, R. J.,
744 Bolt, R. M., Bond, T. C., Dawidowski, L., Kholod, N., Kurokawa, J., Li, M., Liu, L., Lu, Z., Moura, M. C. P.,
745 O'Rourke, P. R., and Zhang, Q. Historical (1750–2014) anthropogenic emissions of reactive gases and aerosols
746 from the Community Emissions Data System (CEDS). *Geosci. Model Dev.* [https://doi.org/10.5194/gmd-11-369-](https://doi.org/10.5194/gmd-11-369-2018)
747 [2018](https://doi.org/10.5194/gmd-11-369-2018) (2018)
- 748 Hourdin, F., Musat, I., Bony, S., Braconnot, P., Codron, F., Dufresne, J.-L., Fairhead, L., Filiberti, M.-A., Friedlingstein, P.,
749 Grandpeix, J.-Y., Krinner, G., LeVan, P., Li, Z.-X., and Lott, F. The LMDZ4 general circulation model: Climate
750 performance and sensitivity to parametrized physics with emphasis on tropical convection. *Clim. Dyn.*
751 <https://doi.org/10.1007/s00382-006-0158-0> (2006)
- 752 Husted, S., and Schjoerring, J. K. Ammonia Flux between Oilseed Rape Plants and the Atmosphere in Response to Changes
753 in Leaf Temperature, Light Intensity, and Air Humidity (Interactions with Leaf Conductance and Apoplastic NH₄⁺
754 and H⁺ Concentrations). *Plant Physiol.* <https://doi.org/10.1104/pp.112.1.67> (1996)
- 755 Jacob, D., Kotova, L., Teichmann, C., Sobolowski, S. P., Vautard, R., Donnelly, C., Koutroulis, A. G., Grillakis, M. G.,
756 Tsanis, I. K., Damm, A., Sakalli, A., and van Vliet, M. T. H. Climate Impacts in Europe Under +1.5°C Global
757 Warming. *Earths Future.* <https://doi.org/10.1002/2017EF000710> (2018)
- 758 Keller, C. A., Long, M. S., Yantosca, R. M., Da Silva, A. M., Pawson, S., and Jacob, D. J. HEMCO v1.0: A versatile,
759 ESMF-compliant component for calculating emissions in atmospheric models. *Geosci. Model Dev.*
760 <https://doi.org/10.5194/gmd-7-1409-2014> (2014)
- 761 Klaes, K. D. The EUMETSAT Polar System. *Comprehensive Remote Sensing.* Elsevier.
762 <https://doi.org/10.1016/B978-0-12-409548-9.10318-5> (2018)
- 763 Krinner, G., Viovy, N., de Noblet-Ducoudré, N., Ogée, J., Polcher, J., Friedlingstein, P., Ciais, P., Sitch, S., and Prentice, I.
764 C. A dynamic global vegetation model for studies of the coupled atmosphere-biosphere system. *Glob. Biogeochem.*
765 *Cycles.* <https://doi.org/10.1029/2003GB002199> (2005)
- 766 Lee, W., An, S., and Choi, Y. Ammonia harvesting via membrane gas extraction at moderately alkaline pH: A step toward
767 net-profitable nitrogen recovery from domestic wastewater. *Chem. Eng. J.*
768 <https://doi.org/10.1016/j.cej.2020.126662> (2020)
- 769 Lentze, G. *Metop-A satellite retiring after 15 years of huge benefits to forecasting* [Text]. ECMWF. ECMWF.
770 [https://www.ecmwf.int/en/about/media-centre/news/2021/metop-satellite-retiring-after-15-years-huge-benefits-](https://www.ecmwf.int/en/about/media-centre/news/2021/metop-satellite-retiring-after-15-years-huge-benefits-forecasting)
771 [forecasting](https://www.ecmwf.int/en/about/media-centre/news/2021/metop-satellite-retiring-after-15-years-huge-benefits-forecasting) (2021, November 12)
- 772 Luo, Z., Zhang, Y., Chen, W., Van Damme, M., Coheur, P.-F., and Clarisse, L. Estimating global ammonia (NH₃)
773 emissions based on IASI observations from 2008 to 2018. *Atmospheric Chem. Phys.* [https://doi.org/10.5194/acp-22-](https://doi.org/10.5194/acp-22-10375-2022)
774 [10375-2022](https://doi.org/10.5194/acp-22-10375-2022) (2022)
- 775 Massad, R.-S., Nemitz, E., and Sutton, M. A. Review and parameterisation of bi-directional ammonia exchange between
776 vegetation and the atmosphere. *Atmospheric Chem. Phys.* <https://doi.org/10.5194/acp-10-10359-2010> (2010)
- 777 Masson-Delmotte, V., P. Zhai, A. Pirani, S.L., Connors, C. Péan, S. Berger, N. Caud, Y. Chen, L. Goldfarb, M.I. Gomis, M.
778 Huang, K. Leitzell, E. Lonnoy, J.B.R., and Matthews, T.K. Maycock, T. Waterfield, O. Yelekçi, R. Yu, and B.
779 Zhou. *IPCC, 2021: Climate Change 2021: The Physical Science Basis. Contribution of Working Group I to the*
780 *Sixth Assessment Report of the Intergovernmental Panel on Climate Change.* Cambridge University Press. In Press.
781 <https://www.ipcc.ch/assessment-report/ar6/> (2021)
- 782 Mattsson, M., B. H., M. D., Loubet, B., M. R., Theobald, M., Sutton, M., Bruhn, D., Neftel, A., and Schjoerring, J. Temporal
783 variability in bioassays of ammonia emission potential in relation to plant and soil N parameters in intensively
784 managed grassland. *Biogeosciences Discuss.* <https://doi.org/10.5194/bgd-5-2749-2008> (2008)
- 785 McDuffie, E. E., Smith, S. J., O'Rourke, P., Tibrewal, K., Venkataraman, C., Marais, E. A., Zheng, B., Crippa, M., Brauer,
786 M., and Martin, R. V. A global anthropogenic emission inventory of atmospheric pollutants from sector- and fuel-
787 specific sources (1970–2017): An application of the Community Emissions Data System (CEDS). *Earth Syst. Sci.*
788 *Data.* <https://doi.org/10.5194/essd-12-3413-2020> (2020)
- 789 Met Office. *Exceptionally warm and dry Spring 2011.* Met Office.
790 [https://www.metoffice.gov.uk/binaries/content/assets/metofficegovuk/pdf/weather/learn-about/uk-past-](https://www.metoffice.gov.uk/binaries/content/assets/metofficegovuk/pdf/weather/learn-about/uk-past-events/interesting/2011/exceptionally-warm-and-dry-spring-2011---met-office.pdf)
791 [events/interesting/2011/exceptionally-warm-and-dry-spring-2011---met-office.pdf](https://www.metoffice.gov.uk/binaries/content/assets/metofficegovuk/pdf/weather/learn-about/uk-past-events/interesting/2011/exceptionally-warm-and-dry-spring-2011---met-office.pdf) (2016)



- 792 Nemitz, E., Sutton, M. A., Schjoerring, J. K., Husted, S., and Paul Wyers, G. Resistance modelling of ammonia exchange
793 over oilseed rape. *Agric. For. Meteorol.* [https://doi.org/10.1016/S0168-1923\(00\)00206-9](https://doi.org/10.1016/S0168-1923(00)00206-9) (2000)
- 794 Olesen, J. E., and Sommer, S. G. Modelling effects of wind speed and surface cover on ammonia volatilization from stored
795 pig slurry. *Atmospheric Environ. Part Gen. Top.* [https://doi.org/10.1016/0960-1686\(93\)90030-3](https://doi.org/10.1016/0960-1686(93)90030-3) (1993)
- 796 Personne, E., Tardy, F., Générumont, S., Decuq, C., Gueudet, J.-C., Mascher, N., Durand, B., Masson, S., Lauransot, M.,
797 Fléchar, C., Burkhardt, J., and Loubet, B. Investigating sources and sinks for ammonia exchanges between the
798 atmosphere and a wheat canopy following slurry application with trailing hose. *Agric. For. Meteorol.*
799 <https://doi.org/10.1016/j.agrformet.2015.03.002> (2015)
- 800 Phillips, S. B., Arya, S. P., and Aneja, V. P. Ammonia flux and dry deposition velocity from near-surface concentration
801 gradient measurements over a grass surface in North Carolina. *Atmos. Environ.*
802 <https://doi.org/10.1016/j.atmosenv.2004.02.054> (2004)
- 803 Pinder, R. W., Gilliland, A. B., and Dennis, R. L. Environmental impact of atmospheric NH₃ emissions under present and
804 future conditions in the eastern United States. *Geophys. Res. Lett.* <https://doi.org/10.1029/2008GL033732> (2008)
- 805 Plumb, R. A., and Stolarski, R. S. Chapter 2: The Theory of Estimating Lifetimes Using Models and Observations. *SPARC*
806 *Lifetimes Rep. 2013 – SPARC Rep. No 6.* https://pages.jh.edu/rstolar1/other_pubs/LifetimeReport_Ch2.pdf (2013)
- 807 Potapov, P., Turubanova, S., Hansen, M. C., Tyukavina, A., Zalles, V., Khan, A., Song, X.-P., Pickens, A., Shen, Q., and
808 Cortez, J. Global maps of cropland extent and change show accelerated cropland expansion in the twenty-first
809 century. *Nat. Food.* <https://doi.org/10.1038/s43016-021-00429-z> (2022)
- 810 Randerson, J. T., Van Der Werf, G. R., Giglio, L., Collatz, G. J., and Kasibhatla, P. S. Global Fire Emissions Database,
811 Version 4.1 (GFEDv4). *ORNL DAAC.* <https://doi.org/10.3334/ORNLLDAAC/1293> (2015)
- 812 Riahi, K., van Vuuren, D. P., Kriegler, E., Edmonds, J., O'Neill, B. C., Fujimori, S., Bauer, N., Calvin, K., Dellink, R.,
813 Fricko, O., Lutz, W., Popp, A., Cuaserna, J. C., Kc, S., Leimbach, M., Jiang, L., Kram, T., Rao, S., Emmerling, J.,
814 ... Tavoni, M. The Shared Socioeconomic Pathways and their energy, land use, and greenhouse gas emissions
815 implications: An overview. *Glob. Environ. Change.* <https://doi.org/10.1016/j.gloenvcha.2016.05.009> (2017)
- 816 Roelle, P. A., and Aneja, V. P. Modeling of Ammonia Emissions from Soils. *Environ. Eng. Sci.*
817 <https://doi.org/10.1089/ees.2005.22.58> (2005)
- 818 Schlesinger, W. H., and Hartley, A. E. A global budget for atmospheric NH₃. *Biogeochemistry.*
819 <https://doi.org/10.1007/BF00002936> (1992)
- 820 Shen, H., Chen, Y., Hu, Y., Ran, L., Lam, S. K., Pavur, G. K., Zhou, F., Pleim, J. E., and Russell, A. G. Intense Warming
821 Will Significantly Increase Cropland Ammonia Volatilization Threatening Food Security and Ecosystem Health.
822 *One Earth.* <https://doi.org/10.1016/j.oneear.2020.06.015> (2020)
- 823 Shephard, M. W., and Cady-Pereira, K. E. Cross-track Infrared Sounder (CrIS) satellite observations of tropospheric
824 ammonia. *Atmos Meas Tech.* <https://doi.org/10.5194/amt-8-1323-2015> (2015)
- 825 Sulla-Menashe, D., and Friedl, M. A. *User Guide to Collection 6 MODIS Land Cover (MCD12Q1 and MCD12C1) Product.*
826 https://lpdaac.usgs.gov/documents/101/MCD12_User_Guide_V6.pdf (2018)
- 827 Svensson, L., and Ferm, M. Mass Transfer Coefficient and Equilibrium Concentration as Key Factors in a New Approach to
828 Estimate Ammonia Emission from Livestock Manure. *J. Agric. Eng. Res.* <https://doi.org/10.1006/jaer.1993.1056>
829 (1993)
- 830 Theobald, M. R., Crittenden, P. D., Hunt, A. P., Tang, Y. S., Dragosits, U., and Sutton, M. A. Ammonia emissions from a
831 Cape fur seal colony, Cape Cross, Namibia. *Geophys. Res. Lett.* <https://doi.org/10.1029/2005GL024384> (2006)
- 832 Tournadre, B., Chelin, P., Ray, M., Cuesta, J., Kutzner, R. D., Landsheere, X., Fortems-Cheiney, A., Flaud, J.-M., Hase, F.,
833 Blumenstock, T., Orphal, J., Viatte, C., and Camy-Peyret, C. Atmospheric ammonia (NH₃) over the Paris megacity:
834 9 years of total column observations from ground-based infrared remote sensing. *Atmospheric Meas. Tech.*
835 <https://doi.org/10.5194/amt-13-3923-2020> (2020)
- 836 USDA. *Europe—Crop Calendars.* *Foreign Agric. Serv. US Dep. Agric.* Foreign Agricultural Service, U.S. Department of
837 Agriculture. https://ipad.fas.usda.gov/rssiws/al/crop_calendar/europe.aspx (2022, May 12)
- 838 Van Damme, M., Clarisse, L., Franco, B., Sutton, M. A., Erisman, J. W., Wichink Kruit, R., van Zanten, M., Whitburn, S.,
839 Hadji-Lazaro, J., Hurtmans, D., Clerbaux, C., and Coheur, P.-F. Global, regional and national trends of atmospheric
840 ammonia derived from a decadal (2008-2018) satellite record. *Environ. Res. Lett.* <https://doi.org/10.1088/1748-9326/abd5e0>
841 (2021)



- 842 Van Damme, M., Clarisse, L., Whitburn, S., Hadji-Lazaro, J., Hurtmans, D., Clerbaux, C., and Coheur, P.-F. Industrial and
843 agricultural ammonia point sources exposed. *Nature*. <https://doi.org/10.1038/s41586-018-0747-1> (2018)
- 844 Van Damme, M., Whitburn, S., Clarisse, L., Clerbaux, C., Hurtmans, D., and Coheur, P.-F. Version 2 of the IASI NH₃
845 neural network retrieval algorithm; near-real time and reanalysed datasets. *Atmos. Meas. Tech.*, 10, 4905–4914,
846 <https://doi.org/10.5194/amt-10-4905-2017> (2017)
- 847 Van Der Molen, J., Beljaars, A. C. M., Chardon, W. J., Jury, W. A., and Faassen, H. G. van. Ammonia volatilization from
848 arable land after application of cattle slurry. 2. Derivation of a transfer model. *Neth. J. Agric. Sci.*
849 <https://doi.org/10.18174/njas.v38i3A.16586> (1990)
- 850 Viatte, C., Abeed, R., Yamanouchi, S., Porter, W., Safieddine, S., Van Damme, M., Clarisse, L., Herrera, B., Grutter, M.,
851 Coheur, P.-F., Strong, K., and Clerbaux, C. NH₃ spatio-temporal variability over Paris, Mexico and Toronto and its
852 link to PM_{2.5} during pollution events. *EGUsphere*. <https://doi.org/10.5194/egusphere-2022-413> (2022)
- 853 Viatte, C., Petit, J.-E., Yamanouchi, S., Van Damme, M., Doucerain, C., Germain-Piaulenne, E., Gros, V., Favez, O.,
854 Clarisse, L., Coheur, P.-F., Strong, K., and Clerbaux, C. Ammonia and PM_{2.5} Air Pollution in Paris during the
855 2020 COVID Lockdown. *Atmosphere*. <https://doi.org/10.3390/atmos12020160> (2021)
- 856 Viatte, C., Wang, T., Van Damme, M., Dammers, E., Meleux, F., Clarisse, L., Shephard, M. W., Whitburn, S., Coheur, P. F.,
857 Cady-Pereira, K. E., and Clerbaux, C. Atmospheric ammonia variability and link with particulate matter formation:
858 A case study over the Paris area. *Atmospheric Chem. Phys.* <https://doi.org/10.5194/acp-20-577-2020> (2020)
- 859 Wentworth, G. R., Murphy, J. G., Gregoire, P. K., Cheyne, C. A. L., Tevlin, A. G., and Hems, R. Soil–atmosphere exchange
860 of ammonia in a non-fertilized grassland: Measured emission potentials and inferred fluxes. *Biogeosciences*.
861 <https://doi.org/10.5194/bg-11-5675-2014> (2014)
- 862 Wesely, M. L. Parameterization of surface resistances to gaseous dry deposition in regional-scale numerical models.
863 *Atmospheric Environ.* 1967. [https://doi.org/10.1016/0004-6981\(89\)90153-4](https://doi.org/10.1016/0004-6981(89)90153-4) (1989)
- 864 Whitburn, S., Damme, M. V., Clarisse, L., Bauduin, S., Heald, C. L., Hadji-Lazaro, J., Hurtmans, D., Zondlo, M. A.,
865 Clerbaux, C., and Coheur, P.-F. A flexible and robust neural network IASI-NH₃ retrieval algorithm. *J. Geophys.*
866 *Res. Atmospheres*. <https://doi.org/10.1002/2016JD024828> (2016)
- 867 Wichink Kruit, R. Surface-atmosphere exchange of ammonia. Ph.D., Wageningen University. Wageningen, Netherlands,
868 <https://edepot.wur.nl/137586> (2010)
- 869 Yang, S., Yuan, B., Peng, Y., Huang, S., Chen, W., Hu, W., Pei, C., Zhou, J., Parrish, D. D., Wang, W., He, X., Cheng, C.,
870 Li, X.-B., Yang, X., Song, Y., Wang, H., Qi, J., Wang, B., Wang, C., ... Shao, M. The formation and mitigation of
871 nitrate pollution: Comparison between urban and suburban environments. *Atmospheric Chem. Phys.*
872 <https://doi.org/10.5194/acp-22-4539-2022> (2022)
- 873 Yu, F., Nair, A. A., and Luo, G. Long-Term Trend of Gaseous Ammonia Over the United States: Modeling and Comparison
874 with Observations. *J. Geophys. Res. Atmospheres*. <https://doi.org/10.1029/2018JD028412> (2018)
- 875 Zhang, L., Wright, L. P., and Asman, W. a. H. Bi-directional air-surface exchange of atmospheric ammonia: A review of
876 measurements and a development of a big-leaf model for applications in regional-scale air-quality models. *J.*
877 *Geophys. Res. Atmospheres*. <https://doi.org/10.1029/2009JD013589> (2010)
- 878